

Final Report

Microgravity Processing of Oxide Superconductors

Grant number: NAG8-1275
NASA Materials Science Discipline
Ground-based research

Grant period: June 1, 1996 – May 31, 2000

Principal investigator:	William H. Hofmeister Department of Chemical Engineering Vanderbilt University Nashville, TN 37235 Phone: 615-322-7053 e-mail: hof@vuse.vanderbilt.edu	
Co-investigator:	Robert J. Bayuzick Vanderbilt University	
Co-investigator:	Marcus Vlasse NASA GMSFC	
Co-investigator:	William McCallum Ames Lab/Iowa State University	
Students supported:	James Olive	M.S., Ph.D.
	David Gustafson	M.S.
	Kosuke Nagashio	visiting student (Tokyo University)
NASA Technical Officer:	Palmer Peters George C. Marshall Space Flight Center Mail Code: SD44	
Monitoring Center:	MSFC	
Task Monitor:	Pat Doty	
Phone:	256 544-4136	
e-mail:	pat.m.doty@msfc.nasa.gov	

Task Objective

The primary goal is to understand the microstructures which develop under the non-equilibrium solidification conditions achieved by melt processing in copper oxide superconductor systems. More specifically, to define the liquidus at the Y-1:2:3 composition, the Nd-1:2:3 composition, and several intermediate partial substitution points between pure Y-1:2:3 and Nd-1:2:3. A secondary goal has been to understand resultant solidification morphologies and pathways under a variety of experimental conditions and to use this knowledge to better characterize solidification phenomena in these systems.

Task Description

Two experimental techniques have been used in these solidification studies: a small drop tube and aero-acoustic levitation (AAL). AAL allows for direct measurement of the sample temperature during processing through optical pyrometry and solidification velocity measurements through high-speed imaging. In drop tube experiments, these measurements are impossible. Therefore, the assumption is made that samples reach the furnace temperature during free-fall. Heat flow calculations on small droplets indicate that this is a reasonable assumption. Solidification events which occur in aero-acoustic levitation experiments also occur in the drop tube experiments. Therefore, correlations are made between the two experiments based on thermal data and microstructural analysis.

After processing, all samples are examined using scanning electron microscopy (SEM) and optical microscopy to determine the phase distributions and morphologies. Transmission electron microscopy (TEM) is used to verify the existence of phases. Electron diffraction in conjunction with TEM provides crystallographic information about the phases present and helps in identification. Powder x-ray diffraction also provides phase information, however samples are crushed for x-ray diffraction and all spatial information is lost. The combination of these five analysis techniques allows for a near complete description of the resulting phase chemistry. This information, coupled with the thermal data, allows determination of the solidification pathways of the material.

Task Significance

There has been little success in producing oxide superconductor materials in bulk which possess suitable properties for technological application. Over the past several years, researchers have used a variety of substitutions to the $\text{YBa}_2\text{Cu}_3\text{O}_{7-8}$ composition in an effort to find a compound which exhibits superior superconducting properties in bulk. The substitution of other rare earth elements for yttrium, either full or partial, has been found to have little or no deleterious effect on electronic properties. However, substitutions do affect the liquidus and phase relations. Lowering the liquidus reduces the maximum processing temperatures and some of the complications of high temperature processing. There is some evidence that these rare earth substitutions increase the width of the superconducting phase from a line compound to a solid solution. Both factors make bulk RE substituted materials more commercially feasible for melt growth.

The difficulties of processing these materials in one g present a clear case for microgravity processing. For example, the large density differences in these multi-component systems cause sedimentation in the melt. Also, $\text{YBa}_2\text{Cu}_3\text{O}_{7-\delta}$ and rare earth (RE) substituted $\text{YBa}_2\text{Cu}_3\text{O}_{7-\delta}$ have a very low thermal conductivity, such that moderate heating and cooling rates develop large thermal gradients in the melt, thereby driving convection. Furthermore, these materials react with all known containing media, but the poor electrical conductivity at room temperature prevents the use of more conventional electromagnetic containerless processing techniques. For various reasons, other techniques for containerless processing are not appropriate because control of the processing environment is crucial to maintaining oxygen stoichiometry and preventing contamination by other gasses such as CO_2 . Furthermore, heat capacity, viscosity and surface tension measurements on the undercooled liquid melt cannot be done on earth but can be obtained in microgravity. Fundamental studies of the melting, undercooling, and solidification behavior under the highly controlled conditions possible in a microgravity environment will lead to a greater understanding of these materials.

Task Progress

In the term of this grant, several important findings were made:

1. The tetragonal 123 phase can be grown directly from the melt by undercooling the liquid.
2. Liquidus temperatures can be determined by drop tube processing.
3. The high temperature phase hierarchy can be modified by rare earth substitutions.
4. A minimum in the liquidus and peritectic transformation temperatures of alloys between pure Nd123 and pure Y123 has been found.
5. Splat-quenching of the undercooled melt forms microcrystalline 123 phases, while splat-quenching at high temperature forms an amorphous phase in Nd rich alloys of 123.

Drop tube experiments were performed at Vanderbilt to determine the high temperature phase relations. Small powders (50 - 100 μm) were processed at different maximum temperatures in a pure oxygen environment. These experiments are used to identify liquidus temperatures and the extent of high temperature solid + liquid regions of the phase diagram. Processed specimens were analyzed using scanning electron microscopy, electron dispersive spectroscopy, and powder x-ray diffraction to characterize microstructures and identify phases. These results have been published in *The Journal of Materials Research*¹, and a figure from that work is presented in figure 1.

¹ Olive, J.R., Hofmeister, W.H., Bayuzick, R.J., and Vlasse M. "High-temperature phase relationships for $\text{Y}_x\text{Nd}_{1-x}\text{Ba}_2\text{Cu}_3\text{O}_y$ ($0.7 < x < 1.0$) superconductors via containerless processing," *J. Mater. Res.*, vol. 14, no. 10, pp. 3843-3850, October 1999.

Olive, J.R., Hofmeister, W.H., Bayuzick, R.J., and Vlasse M. "High-temperature phase relationships for $\text{Y}_x\text{Nd}_{1-x}\text{Ba}_2\text{Cu}_3\text{O}_y$ ($0 < x < 0.5$) superconductors via containerless processing," *J. Mater. Res.*, vol. 14, no. 10, pp. 3851-3858, October 1999.

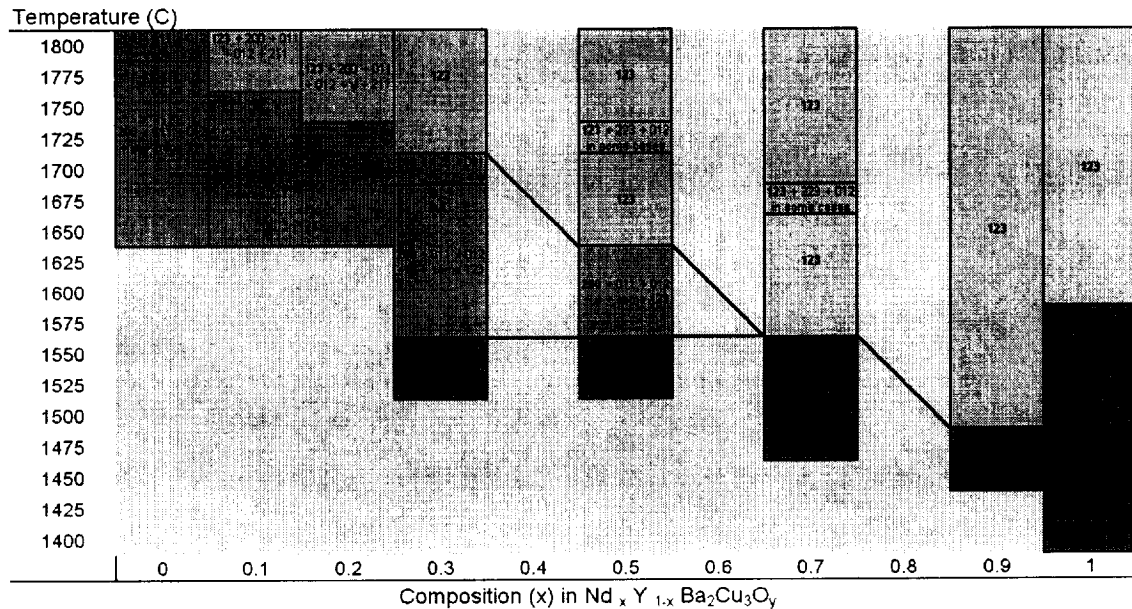


Figure 1: Summary of phases present in drop tube results for processing (Nd, Y)123 alloys. The furnace processing temperatures are on the abscissa and composition on the ordinate.

Containerless melt processing experiments have been performed on the copper oxide superconductors $\text{NdBa}_2\text{Cu}_3\text{O}_{7.8}$ and $\text{GdBa}_2\text{Cu}_3\text{O}_{7.8}$ with rare earth substitutions of Y for Nd in the 123 composition $\text{Nd}_{0.9}\text{Y}_{0.1}\text{-123}$, $\text{Nd}_{0.8}\text{Y}_{0.2}\text{-123}$, $\text{Nd}_{0.7}\text{Y}_{0.3}\text{-123}$, $\text{Nd}_{0.5}\text{Y}_{0.5}\text{-123}$, $\text{Nd}_{0.3}\text{Y}_{0.7}\text{-123}$, $\text{Nd}_{0.2}\text{Y}_{0.8}\text{-123}$, and $\text{Nd}_{0.1}\text{Y}_{0.9}\text{-123}$ as well as several ternary rare earth alloy compositions $\text{Y}_{0.25}\text{Nd}_{0.35}\text{Gd}_{0.40}\text{-123}$, $\text{Y}_{0.50}\text{Nd}_{0.25}\text{Gd}_{0.25}\text{-123}$, and $\text{Y}_{0.75}\text{Nd}_{0.15}\text{Gd}_{0.10}\text{-123}$. These experiments were performed at ISAS in Japan in collaboration with Prof. Kuribayashi of Tokyo University. Starting specimens were 2.5 mm diameter spheres created from stoichiometric 123 sintered powders using a laser copper hearth under flowing oxygen. Spheres were levitated in O_2 using aero-acoustic levitation (AAL), melted with a CO_2 laser, undercooled, and congruently solidified. Recalescence events for the undercooled melts were recorded using two-color pyrometry and a high-speed digital camera. The peritectic transformation temperature for the reaction $\text{RE}_2\text{BaCuO}_5 + \text{liquid} \rightarrow \text{REBa}_2\text{Cu}_3\text{O}_{7.8}$ for each composition was measured. A minimum in the peritectic transformation temperature for the Nd/Y123 alloy system was determined at 1258K for the composition $\text{Y}_{0.3}\text{Nd}_{0.7}\text{Ba}_2\text{Cu}_3\text{O}_{7.8}$. Processed specimens were analyzed using scanning electron microscopy, electron dispersive spectroscopy, and powder x-ray diffraction to characterize microstructures and identify phases. Fully densified 123 was clearly the majority phase with 211 dendrites interspersed near the center of the spheres for all compositions. RE-Ba substitution was not detected during EDS analysis suggesting that 123 is a point compound during the rapid solidification event. According to SEM imaging and XRD results, the volume fraction of 211 in the processed spheres increased as the Y content of the original specimen increased. A periodic shift in the XRD peaks for the 211 phase was also discovered suggesting partial substitution of Nd for Y in this phase under nonequilibrium melt processing conditions. A paper of this work is in review by The Journal of Materials Research. A pre-print is included in appendix A.

Splat quenching experiments were also conducted on Nd123, and Gd123 in Ar using AAL at Containerless Research in Chicago. Experiments were conducted to make splats above the liquidus and on liquid undercooled below the peritectic temperature. Microstructural characterization of samples by SEM indicates the presence of amorphous phase in the samples splatted above the liquidus. High temperature XRD analysis conducted in dry air revealed the formation of BaCO_3 at 400 °C and Nd123 phase formed at 700 °C by solid diffusion. Sample structure is presently being analyzed using a channel patterning technique. For splats made below the peritectic, the morphology of the Nd123 phase changed from planar to cellular/dendritic with decreasing growth velocity along the thermal gradient. Nd422 dendrites were also identified and formed because of the increased interface temperature of Nd123 near the center of the splat. The planar front observed suggests that the growth of Nd123 had attained a maximum growth velocity near the absolute stability criterion. This work has been published² in The Journal of Materials Research, and a pre-print is included in appendix B.

² "Formation of $\text{NdBa}_2\text{Cu}_3\text{O}_{7-d}$ amorphous phase by combining aero-acoustic levitation and splat quenching," K. Nagashio, W. H. Hofmeister, D. E. Gustafson, A. Altgilbers, R. J. Bayuzick and K. Kuribayashi, to be published J. Mater. Res., Vol. 16, No. 1, Jan 2001.

Appendix A

Formation of $\text{Y}_x\text{Nd}_{1-x}\text{Ba}_2\text{Cu}_3\text{O}_{7-\delta}$ ($0 \leq x \leq 0.9$) superconductors from an undercooled melt via aero-acoustic levitation

D.E. Gustafson, W.H. Hofmeister, and R.J. Bayuzick

Department of Chemical Engineering, Vanderbilt University, Nashville, Tennessee 37235, USA

K. Nagashio and K. Kuribayashi

The Institute of Space and Astronautical Science, Sagami-hara, Kanagawa 229-8510, JAPAN

ABSTRACT

This paper presents the results of rapid solidification experiments performed on the copper oxide superconductors $\text{Y}_x\text{Nd}_{1-x}\text{Ba}_2\text{Cu}_3\text{O}_{7-\delta}$ ($0 \leq x \leq 0.9$). Spherical rare earth (RE) 123 specimens were levitated in O_2 using aero-acoustic levitation, melted with a laser, undercooled, and solidified.

The peritectic transformation temperature for the reaction $\text{RE}_2\text{BaCuO}_5 + \text{liquid} \rightarrow \text{REBa}_2\text{Cu}_3\text{O}_{7-\delta}$ corresponding to the maximum recalescence temperature during solidification was determined.

RE123 was formed directly from the melt for Y-Nd binary alloy compositions with Nd concentration greater than 20% (Y concentration less than 80%). A minimum in the peritectic transformation temperature for the Nd/Y123 system corresponding to a composition $\text{Y}_{.3}\text{Nd}_{.7}\text{123}$ was determined at 66°C below the peritectic of pure Nd123.

INTRODUCTION

Melt processing of rare earth (RE) 123 superconductors has gained importance in recent years. While the first high temperature superconductors (HTSCs) were made using traditional ceramic press and sinter technology, recent fabrication efforts have employed alternate processing techniques including laser ablation and ion beam assisted deposition for thin film fabrication of tapes and wires and melt growth for bulk materials.¹⁻⁴ To optimize these techniques and identify other potential processing strategies, phase relation studies on HTSCs have been conducted on a wide variety of superconducting compounds using numerous processing strategies. Studies performed to date have contributed to the understanding of high temperature phase relationships, enabled the measurement of the thermophysical properties of liquids and solid-liquid phase mixtures, and yielded transformation temperatures and enthalpy values. The data obtained has enhanced the understanding of these complex systems and has helped identify processing capabilities for HTSCs. However, the research to date has failed to achieve a breakthrough for wide spread application of these materials. To overcome drawbacks of the sintered material, many researchers have developed new processing routes involving melt-processing techniques. Melt processing has significantly advanced the state-of-the-art understanding of superconductivity in polycrystalline bulk materials and has produced materials with critical current (J_c) of greater than 10^4 A/cm².⁵ The melt processed materials produced, however, suffer from several shortcomings. Due to incongruent melting of RE123 at high temperatures, liquid phase flows out of the interior of the material resulting in voids, and Ba-Cu-O liquid inclusions may become trapped between grains reducing superconductive properties. Processing rates are typically very slow with melt processing, i.e. on the order of 50 mm/h for a 25 mm² cross sectional area sample.⁶ Slow processing rates can also expose the material to moisture and CO₂ which are highly reactive with copper oxide superconductors.⁷ Also,

distortions and macrocracks form due to severe shrinkage accompanying the melt processing. Large complex shapes are therefore difficult to fabricate by melt processing and the only shapes reported to date have been either disks or bars.⁸

Several researchers have examined the effect of mixed RE atoms in the 123 system referred to as RE123 alloys. Work to date has included oxygen-controlled-melt-growth of RE123 alloys, containerless drop tube processing of RE123 alloys, and directional solidification of RE123 alloys.⁹⁻¹³ Interesting results include a sharper critical temperature (T_c) as well as a higher J_c in the alloy compared to the single RE system. Additionally, the liquidus for $Y_xNd_{1-x}Ba_2Cu_3O_{7-8}$ was measured by J.R. Olive during drop tube processing experiments in O_2 , and a minimum liquidus temperature for the rare earth oxide + liquid region in the system was found at 1500°C ($\pm 25^\circ\text{C}$) corresponding to the composition $Y_{.1}Nd_{.9}Ba_2Cu_3O_{7-8}$.¹⁴

EXPERIMENTAL METHOD

This study examines the role of full to partial substitution of Nd in the Y123 structure under rapid solidification conditions. Aero-acoustic levitation (AAL) was used to levitate and undercool Nd123 along with a range of pseudo-binary rare earth combinations $Y_xNd_{1-x}123$ ($x = 0.9, 0.8, 0.7, 0.5, 0.3, 0.2, 0.1$). Specimens were melted to the fully liquid state (above the rare earth oxide liquidus) by a CO_2 laser in flowing O_2 . Solidification structures were examined using scanning electron microscopy, electron dispersive spectroscopy, and powder x-ray diffraction to characterize microstructures and identify phases.

Starting powders of orthorhombic RE123 were supplied by Superconductive Components, Inc., fabricated using standard ceramic press and sinter techniques. Levitation spheres were then fabricated in a copper hearth under flowing O_2 . The aero-acoustic levitator (AAL) consisted of an O_2 gas jet coupled with a three-axis acoustic positioning system for levitation of samples.¹⁵

The O₂ gas jet was pre-heated to approximately 400°C in the AAL. Melting of samples was accomplished using a Rofin-Sinar 1700 SM CO₂ laser. The laser beam was split and focused onto opposing sides of each specimen, perpendicular to the gas jet flow. Samples were 2 mm diameter spheres having a mass of 30-50 mg. A typical experiment involved levitating the sample in the O₂ gas jet and heating it with the laser until liquid vortex currents were visible on the surface. After several seconds, the laser beam was shut off and the sample allowed to radiantly cool at 300-400°C/s. Temperature measurements were made using a two-color pyrometer with Si and InGaAs detectors, and recalescence events were recorded using a Kodak EKTAPRO HS Motion Analyzer Model 4540 operating at 4500 frames/s.

RESULTS

Figure 1 is a secondary electron image of a typical sphere that was processed in the AAL. Black globules are Ba-Cu-O and are typically hollow. The lightly colored regions are faceted regions of RE123. Samples were melted by the laser while being levitated and were undercooled several hundred degrees relative to the liquidus before solidification. Solidification of the samples was accompanied by a distinct recalescence event. This event lasted between 0.2 and 0.3 seconds and the increased emissive intensity was visible to the naked eye. Solidification events varied considerably in duration and intensity depending upon the composition of the sample, but the general solidification process appears to be similar. After the laser was blocked and the sample cooled a few seconds where the surface temperature was approximately the RE123 peritectic transformation temperature (T_p^{123}), particles or islands of RE123, roughly 100 μm in size were seen floating on the surface of the levitated melt. These particles increased in number as the bulk liquid undercooling (relative to T_p^{123}) increased. Eddies in the swirling melt were observed drawing the particles to a preferred location near the top of the sphere. With further

cooling, the particles continued to cluster until a solid front was seen growing from the top to the bottom of the spherical surface. This front wrapped around the surface of the sphere, enveloping the melt with a shell of solid material. The recalescence event occurred simultaneously in the bulk of the sample and was marked by a distinct flash of light. This entire scenario occurred in less than 400 ms. Solidification events recorded by the Kodak EKTAPRO camera confirmed these observations. The as-solidified morphology of samples fully melted in the AAL can be generalized into three zones. Typically, the solidification of undercooled powders results in a dual zone microstructure; an adiabatic zone from solidification due to undercooling and a zone where solidification is controlled by external heat flow.¹⁶ Figure 2 is a collection of micrographs depicting the three different zones typically found in the microstructures of processed samples. In Figure 3 a schematic of the hypothesized temperature profiles in the drop is presented for clarification. The first zone encompasses the outer layer of the sphere, which solidified first. Here, solidification of the melt proceeded quickly. This outer zone is composed of relatively void-free RE123, and the morphology can be described as faceted. The formation of this layer involved the recalescence event recorded by the pyrometer and EKTAPRO camera. The thickness of this outer layer appears to be a function of composition and varied from a maximum of 500 μm for the Nd rich samples to 200 μm and less for the Y rich samples. In this region, the sample was undercooled relative to T_p^{123} , and RE123 formed directly from the undercooled melt (curve t1 in Figure 3). The undercooling was limited due to heterogeneous nucleation from the islands of RE123 phase on the surface of the melt. The adiabatic growth of the RE123 raised the drop temperature to T_p^{123} in zone 1, and limited further growth of RE123 (t2 in Figure 3). The second zone, which lies between the outer zone and the center of the sphere, is a relatively thin transitional region where RE211 dendrites are surrounded by RE123 dendrites. The RE211 dendrites in this region nucleated heterogeneously at the interface of the solid RE123 and the

melt. The undercooling relative to the RE211 peritectic transformation temperature (T_p^{211}), which is greater than T_p^{123} , drove RE211 solidification (curve t3 in Figure 3). The dendrites were initially fine, but coarsened closer to the center of the sphere as the undercooling (relative to T_p^{211}) diminished (up to t4 in Figure 3). Thus, in these samples there are two adiabatic solidification zones. As the drop cooled by external heat transfer, the RE211 + liquid \rightarrow RE123 peritectic transformation is evidenced. The third zone is located near the center of the sphere generally adjacent to the shrinkage voids, and is dominated by coarse RE211 dendrites with interdendritic Ba-Cu-O. This final zone was formed as the sphere continued to cool due to the rate of external heat flow, and the microstructure indicates solidification of zone 3 without significant undercooling (curve t5 in Figure 3). Due to the moderate cooling rate, the remaining Ba-Cu-O liquid was unable to react with the RE211 to form RE123, and solidified around the RE211 dendrites. Figure 4 is a collection of secondary electron images for samples with varying composition, which depict the RE123 and RE211 microstructures typically examined in this study.

Two Y rich compositions failed to melt completely and, therefore, did not exhibit recalescence behavior upon cooling: $Y_{.9}Nd_{.1}123$, and $Y_{.8}Nd_{.2}123$. The high liquidus temperatures ($\sim 1750^\circ\text{C}$) for these samples prohibited complete melting in the AAL. The solidification structures observed in these Y rich samples contained large, faceted rare earth oxide particles and a mixture of Ba-Cu-O phases indicating that the samples were in the rare earth oxide + liquid region of the phase diagram when the laser was blocked and the samples quenched.

DISCUSSION

Containerless processing with aero-acoustic levitation allows for cooling of molten RE123

alloy samples several hundred degrees below the RE oxide liquidus until spontaneous crystallization or recalescence occurs. Cooling curves for processed samples reveal characteristic events, which correspond to the release of the latent heat of fusion and result in the heating of the samples to T_p for RE123. Analysis of the microstructure confirms the adiabatic solidification of RE123, so the maximum recalescence temperature was assumed to correspond to T_p for each composition.

In this work, the uncorrected recalescence temperature for Nd123 was indicated to be 1043°C ($\pm 17^\circ\text{C}$). This indicated temperature is below the previously reported value of T_p for Nd123 by 66°C. Prado et al. report the T_p to be 1109°C for Nd123 in pure oxygen.¹⁷ Kambara et al. report the T_p for Nd123 in oxygen to be 1112°C.¹⁸ The absolute differences between the reported values and the experiments detailed in this report are attributed to error in the pyrometer which was used to measure temperature in the experiments reported here. This disagreement could not be experimentally confirmed because the pyrometer failed prior to independent calibration. However, by using the difference between the experimental and reported T_p for Nd123 as an in-situ calibration factor, the experimental recalescence temperatures were corrected by this fixed amount to reflect the actual transformation temperatures for the compositions studied in this work.

Figure 5 is a plot of the peritectic recalescence temperatures obtained in this report. Error bars representing one standard deviation for multiple experiments with each corresponding composition have been included. These results are also plotted with the liquidus for the Y-Nd alloys for illustration in Figure 6.¹⁷ The minimum in the liquidus corresponds to a composition of $\text{Y}_{1.1}\text{Nd}_{9.123}$ while the minimum in T_p corresponds to $\text{Y}_{3.1}\text{Nd}_{7.123}$. The minimum in undercooling relative to the rare earth oxide liquidus observed in these experiments, however, corresponds to 420°C (corrected) for samples with composition $\text{Y}_{2.1}\text{Nd}_{8.123}$ and $\text{Y}_{1.1}\text{Nd}_{9.123}$. Thus the range of

compositions, which undercooled less than 500°C to form RE123 directly from the melt, extends from Nd123 to $Y_{0.3}Nd_{0.7}123$. The degree of undercooling for Nd123 to $Y_{0.3}Nd_{0.7}123$ samples corresponds to approximately 30% of the liquidus. Compositions more rich in Y undercooled more than 650°C below the liquidus to form RE123 directly from the melt, but a considerably larger volume fraction of RE211 appears in these specimens than in Nd rich specimens. The degree of undercooling for the Y rich specimens was over 40% of the liquidus indicating that it is more difficult to form RE123 from the melt for Y rich compositions.

Undercooling and rapid solidification are known to alter materials by refining microstructural features and modifying the thermodynamic and kinetic parameters affecting phase selection. Many ceramics including the RE123 system possess a high entropy of fusion because of their complex crystal structures, and pure ceramics tend to exhibit faceted dendritic growth at high undercoolings. Ceramics also have low thermal conductivity, and the resulting thermal gradients may cause the surface and the center of samples to have radically different temperatures. Throughout this study, faceted dendrites of RE123 were found in abundance in samples which undercooled prior to solidification. The solidification structures, however, are varied and complex because of the variation in degree of undercooling and thermal gradients. In compositional analysis by EDS in this work, the RE ratios in solidification structures analyzed were the same as the nominal starting composition of the alloy confirming good mixing and distribution of the RE species in the melt prior to solidification.

Pyrometry evidence seems to indicate that the volume fraction of RE123 formed directly from the melt increased as the Nd content in the Y-Nd composition increased. The compositional dependence of phase selection is clearly evident from a qualitative review of characteristic sample micrographs and is also evident from a comparison of x-ray diffraction spectra. Figure 7 is a comparative plot of XRD data for several Y-Nd alloys. The large volume fraction of RE123

for all samples is readily seen. Also, prevalent is the appearance of RE211 peaks in the Y rich alloys. The large degree of undercooling required creates larger thermal gradients in the Y rich samples than the Nd rich samples. Thus, processing in the AAL resulted in formation of RE 123 directly from the melt only in an outer shell of the Y rich samples. The phase stability of RE211 may also play a role in this outcome since RE211 is not a stable phase in the Nd123 system. Increasing the Y content may create favorable conditions for the formation of RE211 during rapid solidification processing in the AAL or in drop tubes^{14,19}. The Nd rich alloys have no appreciable second phases or byproducts formed indicating that the formation of RE123 is favored in the rapid solidification of a melt with a Nd rich RE123 starting composition. Peaks corresponding to the Pt heater, which was present in the x-ray diffractometer, are found in all XRD spectra in this report.

Previous processing studies of RE123 at near equilibrium conditions in high oxygen environments resulted in the partial substitution of RE^{3+} for Ba^{2+} and the formation of compounds with the formula $\text{RE}_{1+x}\text{Ba}_{2-x}\text{Cu}_3\text{O}_{7-\delta}$.²⁰ This solid solubility behavior was determined to be undesirable since the RE123 solid solutions have inferior superconducting properties compared to the stoichiometric compounds.²¹ Low oxygen partial pressure environments were used to avoid solid solution formation in near equilibrium melt processing because the substitution of RE^{3+} for Ba^{2+} must be compensated by the addition of extra oxygen. Simply removing the oxygen removed the opportunity for solid solution formation in those near-equilibrium processing techniques. In this study, no evidence of substitution of Nd^{3+} for Ba^{2+} was discovered even while processing the samples in pure oxygen. Thus it appears possible to solidify RE123 directly from the melt while effectively bypassing the formation of solid solutions using rapid solidification techniques in atmospheric oxygen pressure.

RE123 studies performed to date have found substitution of many RE atoms for Y in the 123-crystal structure. The substitution of a single RE atom for Y in the 123 structure causes small distortions in the lattice parameters depending upon the size of the RE atom, but the substitution has no discernible effect on the superconducting properties of orthorhombic 123. Additionally, analysis of samples processed in AAL has verified that RE atom ratios in RE211 particles are similar to the nominal starting composition. The RE211 crystal is orthorhombic but contains two RE atoms per unit cell. The role of the RE211 phase in flux pinning has been speculated, and the formation of RE211 in a pseudo-binary alloy system warrants further discussion. Other RE ions substitute readily for Y in this structure to form RE211, but the structure of Nd422 is radically different due to the large size of the Nd^{3+} ion. The Nd^{3+} ion has been reported to be too large to be accommodated in the Y211 crystal structure.²² Compositionally, EDS scans indicate that the RE211 phases formed during AAL processing has a RE composition (Nd/Y ratio) the same as the nominal starting composition. Since substitution of Nd^{3+} in the Y211 structure would result in an increase in the lattice parameters of the Y211 cell, an identifiable x-ray shift should also accompany substitution. Also, the degree of shift should be proportional to the Nd content of the nominal starting composition. Figure 8 is a plot of 2θ versus the RE^{3+} average ionic radius for the planes of highest diffraction intensity for RE211 phases (RE = Dy, Er, Eu, Gd, Ho, Sm, Y, and Yb) from powder diffraction data as well as experimental data from this report.²³ The experimental data was obtained from XRD plots for a number of compositions studied in this report, and the average ionic radius was determined using the ratio of RE^{3+} atoms in the starting sample. Additionally, the theoretical 2θ predicted using a hard sphere model of the RE211 unit cell with increased size due to substitution of Nd^{3+} for Y^{3+} is plotted. The trend appears to be well developed and in good agreement with experimental data indicating that increasing the size

of the RE211 unit cell by substitution of Nd^{3+} for Y^{3+} is possible under rapid solidification conditions.

CONCLUSIONS

Aero-acoustic levitation is a useful technique for melting, undercooling, and rapidly solidifying high temperature ceramic oxide superconductors. In this study, binary Nd/Y RE123 samples were melted, undercooled hundreds of degrees relative to the liquidus, and solidified to form RE123 for compositions with Nd concentration greater than 20% (Y concentration less than 80%). Mixtures of Y123 and Nd123 resulted in a minimum for the peritectic temperature at $\text{Y}_{0.3}\text{Nd}_{0.7}\text{RE}_{123}$, 66°C below the peritectic of pure Nd123. It was also determined that increasing the Nd content in Nd/Y alloys resulted in the formation of a higher volume fraction of RE123. Nd-Ba solid solution behavior of the type $\text{Nd}_{1+x}\text{Ba}_{2-x}\text{Cu}_3\text{O}_{7-\delta}$ was not observed in this study, and the RE ratio in RE123 and RE211 structures formed during AAL processing mirrored the nominal starting composition of the bulk. Lastly, significant changes occur in the RE211 lattice parameters because of Nd substitution for Y in the Y211 unit cell.

ACKNOWLEDGMENTS

This work was supported by the National Aeronautics and Space Administration Office of Microgravity Science and Applications Division, Grant No. NAG8-1275. The authors appreciate the support of the Japanese Institute of Space and Astronautical Science in supporting the experimental work.

REFERENCES

1. J.R. Hull, JOM 51, 7, 12 (1999).
2. A. Goyal, R. Feenstra, F.A. List, M. Paranthanman, D.F. Lee, D.M. Kroeger, D.B. Beach, J.S. Morrell, T.G. Chirayil, D.T. Verebelyi, X. Cui, E.D. Specht, D.K. Christen, and P.M. Martin, JOM 51, 7, 12 (1999).
3. S. Foltyn, P. Tiwari, R. Dye, M. Le, and X. Wu, Appl. Phys. Lett. **63** 1848-50 (1993).
4. Y. Iijima, N. Tanabe, O. Kohno, and Y. Ikeno, Appl. Phys. Lett. **60** 769-771 (1992).
5. S. Jin, T.H. Tiefel, R.C. Sherwood, M.E. Davis, R.B. van Dover, G.W. Kammlott, R.A. Fastnacht, and H.D. Keith, Appl. Phys. Lett. **52** 2074 (1988).
6. K. Salama A.S. Parikh, and L. Woolf, Appl. Phys. Lett. **68** 14, 1993-1995 (1996).
7. M. Murakami, Appl. Supercond. 6, 2-5, 51-59 (1998).
8. E.S. Reddy, T. Rajasckharan, G.R. Kumar, T.V. Chandrasekhar Rao, V.C. Sahni, Mater. Sci. Eng. B57, 179-185 (1999).
9. J.M.S. Skakle, Mat. Sci. Eng. R23, 1-40 (1998).
10. M. Boffa, A Di Trollo, S. Pace, A. Saggese and A. Vecchione, IEEE Trans. Appl. Supercond. 7, 2 (1997).
11. M. Muralidhar and M. Murakami, Appl. Supercond. 5, 1-6, 127-131 (1997).
12. J.R. Olive, Ph.D. Dissertation, Vanderbilt University (1998).
13. T. Saitoh, K. Segawa, K. Kamada, N. Sakai, T. Segawa, S.I. Yoo, and M. Murakami, Physica C 288, 141-147 (1997).
14. J.R. Olive, W.H. Hofmeister, R.J. Bayuzick, and M. Vlasse, J. Mater. Res. 14, 10, 3851-58 (1999).
15. J.K.R. Weber, D.S. Hampton, D.R. Merkley, C.A. Rey, M.M. Zatarski, and P.C. Nordine, Ceram. Bull. 70, 1, 71 (1991).
16. C.G. Levi and R. Mehrabian, Met. Trans. 13A, 221 (1982).
17. F. Prado, A. Caneiro, and A. Sequis, Physica C 295, 235-246 (1998).
18. M. Kambara, M. Nakamura, Y. Shiohara, and T. Umeda, Physica C 275, 127-134 (1997).
19. J.R. Olive, W.H. Hofmeister, R.J. Bayuzick, and M. Vlasse, J. Mater. Res. 14, 10, 3851-58 (1999).
20. M. Murakami, S.I. Yoo, T. Higuchi, N. Sakai, J. Weltz, N. Koshizuka, and S. Tanaka, Jpn. J. Appl. Phys. 33, L715 (1994).
21. M. Kambara, T. Umeda, M. Tagami, X. Yao, E.A. Goodilin, and Y. Shiohara, J. Am. Ceram. Soc. 81 [8] 2116 (1998).
22. W. Wong-Ng, L.P. Cook, B. Paretzking, M.D. Hill, and J.K. Stalick, J. Am. Ceram. Soc. 77 [9] 2354-62 (1994).
23. R.D. Shannon, Acta Cryst. A32, 751 (1976).

Figure Captions

Figure 1. Secondary electron micrograph showing the surface of a typical sphere processed in the AAL. Black globules are Ba-Cu-O and the light colored regions are faceted RE123.

Figure 2. Collection of secondary electron images from a Y_3Nd_7 123 sample depicting (a) relatively void-free RE123 faceted dendrites at the outer edge of the sphere, (b) the second zone where RE211 dendrites form at the boundary of RE123 faceted particles, and (c) the inner zone comprised of RE211 dendrites with interdendritic Ba-Cu-O adjacent to the shrinkage cavity.

Figure 3. Schematic temperature profiles for solidification of the drops are shown at arbitrary times (t1-t5). Curve t1 shows the recalescence of the surface region to the RE123 peritectic transformation temperature. RE123 grew adiabatically until the driving undercooling for solidification was overcome by the release of latent heat of fusion in t2. At this point, RE211 is undercooled with respect to T_p^{211} , and this phase nucleated on the RE123 phase and grew adiabatically until time t4, whereupon the solidification was controlled by external heat transfer.

Figure 4. Secondary electron images of several samples processed in the AAL. The large fraction of RE123 is evident in each micrograph. RE211 increases with increasing Y content of the bulk. (a). Cross-section of a sample with composition $Y_1Nd_9Ba_2Cu_3O_{7-\delta}$. (b). Cross-section of a sample with composition $Y_3Nd_7Ba_2Cu_3O_{7-\delta}$. (c). Cross-section of a sample with composition $Y_5Nd_5Ba_2Cu_3O_{7-\delta}$. (d). Cross-section of a sample with composition $Y_7Nd_3Ba_2Cu_3O_{7-\delta}$.

Figure 5. Experimentally determined average peritectic temperatures for Nd/Y123 binary alloy samples processed in the AAL. The temperature has been corrected using Nd123 as an in-situ calibration. The standard deviation in the data for multiple experiments with the same composition was used to calculate the magnitude of the error bars.

Figure 6. Trace of the Nd/Y123 liquidus and peritectic in pure O_2 . Liquidus temperatures were obtained from drop tube work performed by Olive and peritectic temperatures represent corrected experimental data from this work.¹³

Figure 7. A compilation of XRD spectra for Y/Nd123 alloys processed in the AAL. RE123 is the dominant phase for all compositions. The appearance of RE211 in the scans becomes more prevalent in Y-rich compounds. The Pt peak is from the heating fixture in the XRD.

Figure 8. Comparison of the 2θ values for highest intensity diffraction planes for RE211 from powder diffraction files (RE = Dy, Er, Eu, Gd, Ho, Sm, Y, and Yb) with values from experimental data and theoretical values for Nd211 calculated from a simple model.

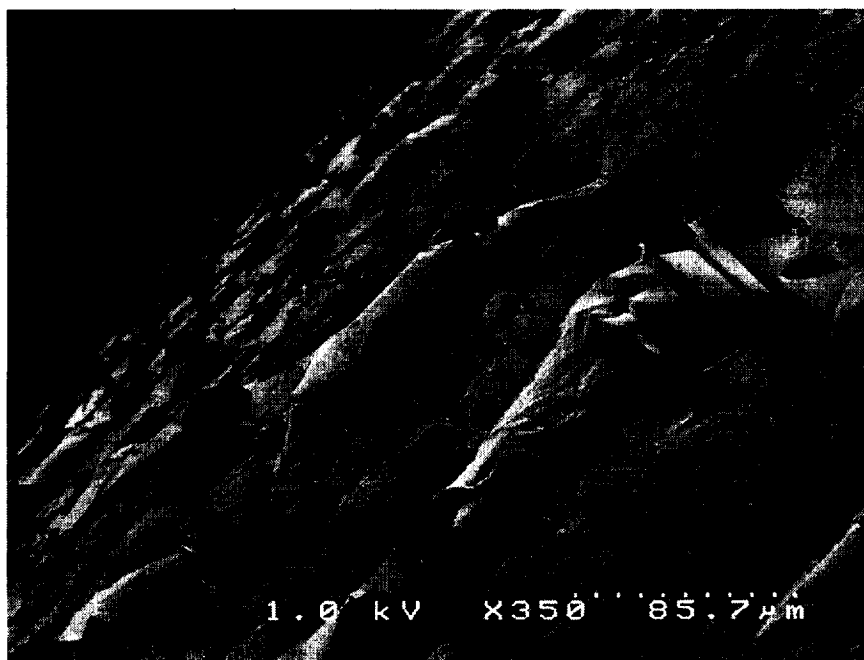


Figure 1. Secondary electron micrograph showing the surface of a typical sphere processed in the AAL. Black globules are Ba-Cu-O and the light colored regions are faceted RE123.

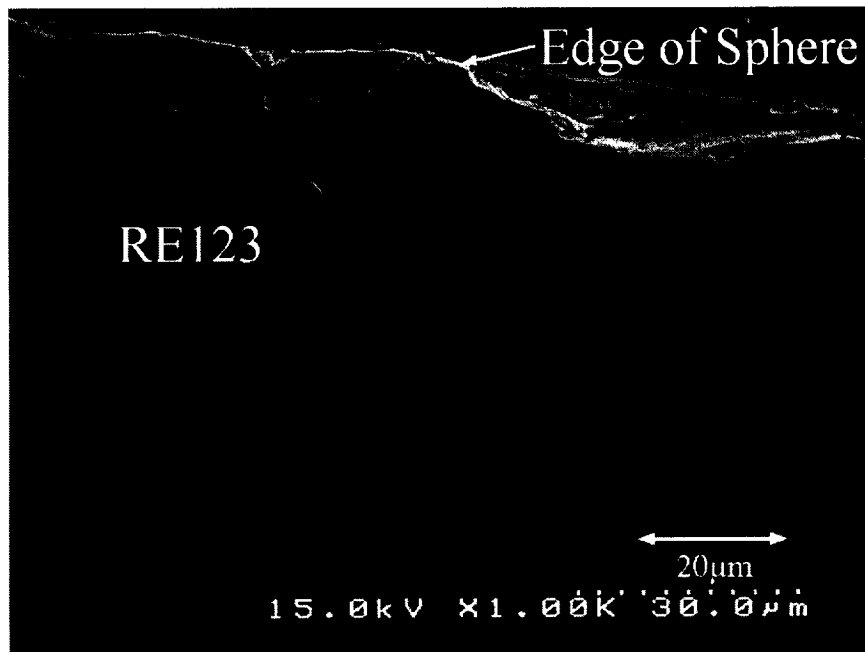


Figure 2(a). Relatively void-free RE123 faceted dendrites at the outer edge of the sphere.

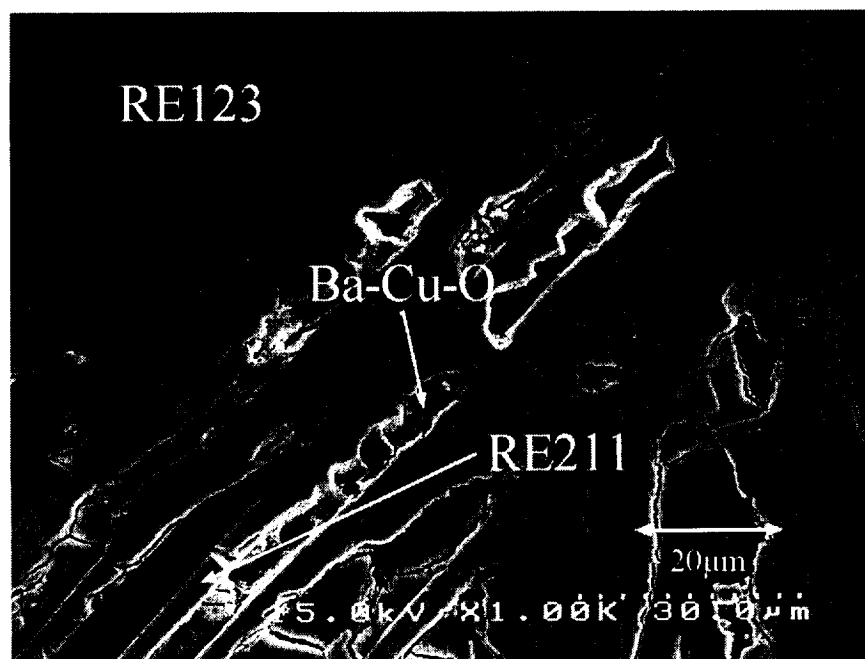


Figure 2(b). The second zone with RE211 dendrites at the boundary of RE123 faceted dendrites.

Figure 2. Collection of secondary electron images from a $Y_3Nd_{71}23$ sample depicting (a) relatively void-free RE123 faceted dendrites at the outer edge of the sphere, (b) the second zone where RE211 dendrites form at the boundary of RE123 faceted particles, and (c) the inner zone comprised of RE211 dendrites with interdendritic Ba-Cu-O adjacent to the shrinkage cavity.

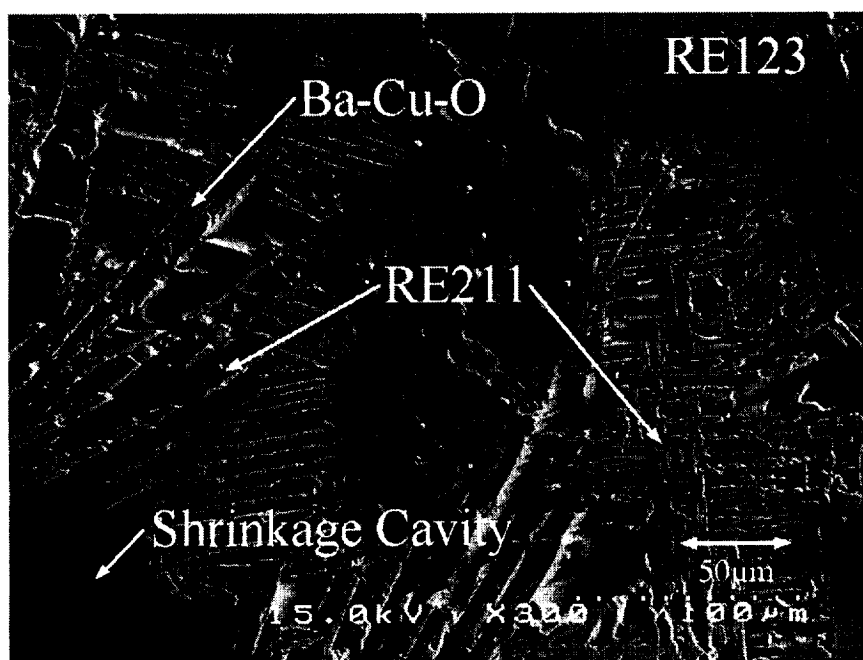


Figure 2(c). The inner zone comprised of RE211 dendrites with interdendritic Ba-Cu-O adjacent to the shrinkage cavity.

Figure 2. Collection of secondary electron images from a Y_3Nd_7123 sample depicting (a) relatively void-free RE123 faceted dendrites at the outer edge of the sphere, (b) the second zone where RE211 dendrites form at the boundary of RE123 faceted particles, and (c) the inner zone comprised of RE211 dendrites with interdendritic Ba-Cu-O adjacent to the shrinkage cavity.

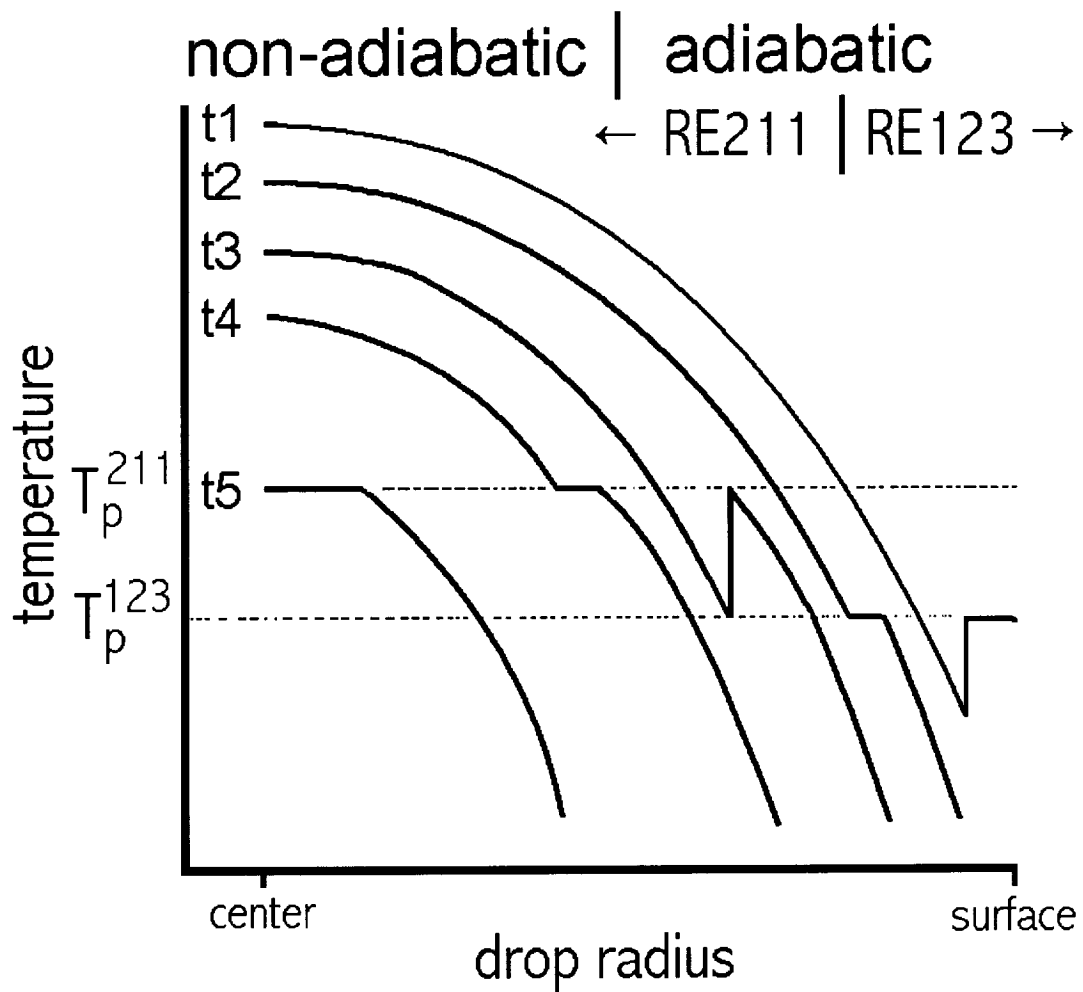


Figure 3. Schematic temperature profiles for solidification of the drops are shown at arbitrary times (t_1 - t_5). Curve t_1 shows the recalescence of the surface region to the RE123 peritectic transformation temperature. RE123 grew adiabatically until the driving undercooling for solidification was overcome by the release of latent heat of fusion in t_2 . At this point, RE211 is undercooled with respect to T_p^{211} , and this phase nucleated on the RE123 phase and grew adiabatically until time t_4 , whereupon the solidification was controlled by external heat transfer.

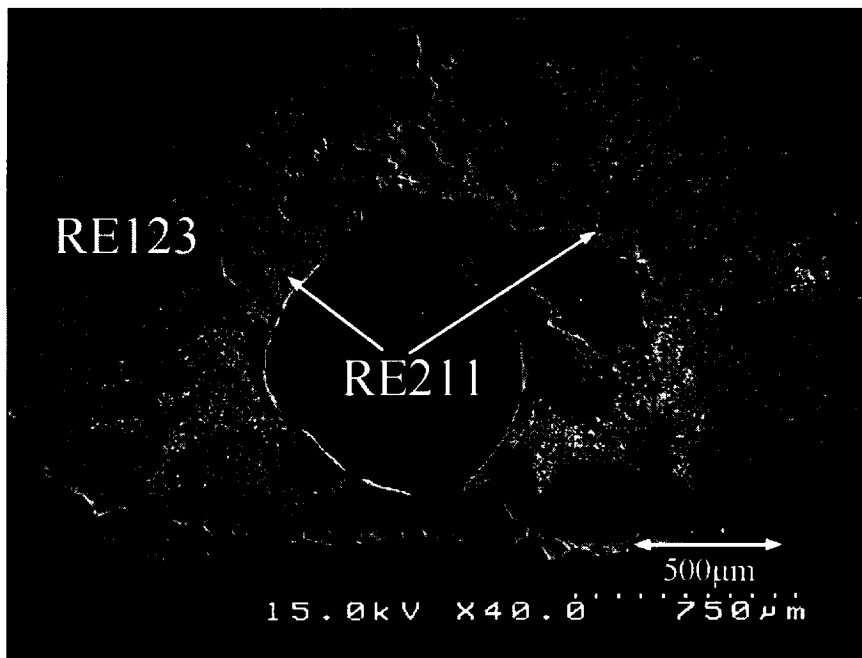


Figure 4(a). Cross-section of a sample with composition $\text{Y}_{1.1}\text{Nd}_{9.9}\text{Ba}_2\text{Cu}_3\text{O}_{7-\delta}$.

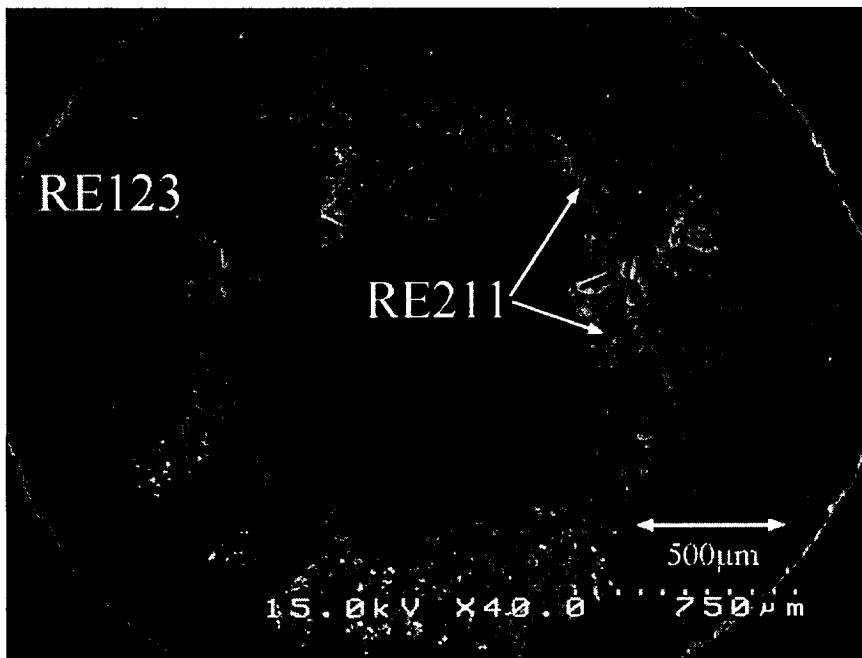


Figure 4(b). Cross-section of a sample with composition $\text{Y}_{3.3}\text{Nd}_{7.7}\text{Ba}_2\text{Cu}_3\text{O}_{7-\delta}$.

Figure 4. Secondary electron images of several samples processed in the AAL. The large fraction of RE123 is evident in each micrograph. RE211 increases with increasing Y content of the bulk.

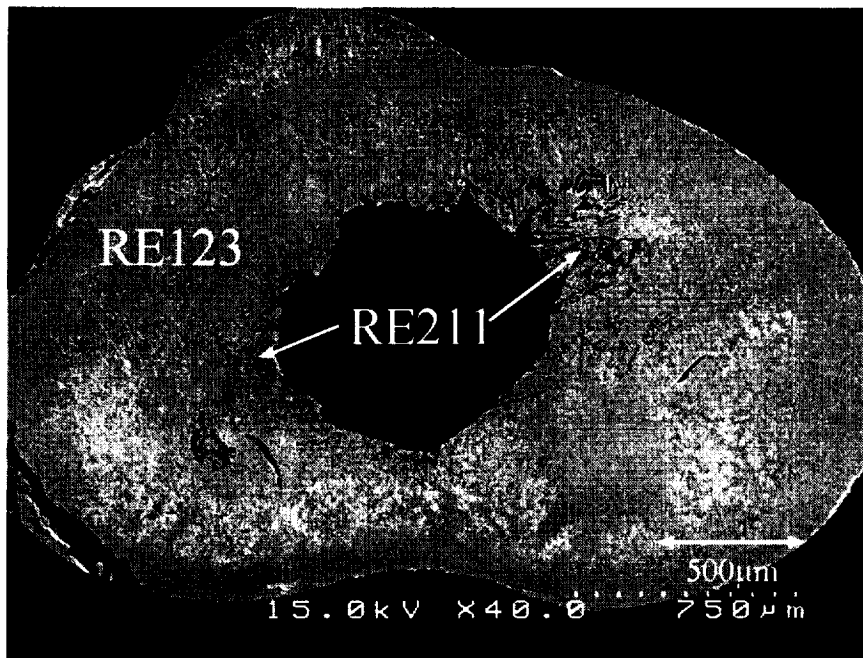


Figure 4(c). Cross-section of a sample with composition $\text{Y}_5\text{Nd}_5\text{Ba}_2\text{Cu}_3\text{O}_{7-\delta}$.

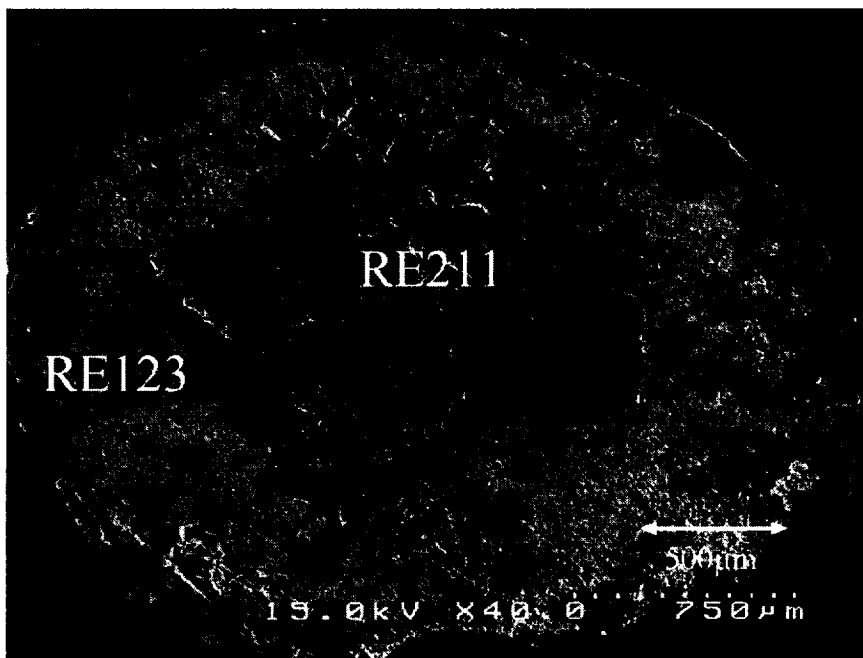


Figure 4(d). Cross-section of a sample with composition $\text{Y}_7\text{Nd}_3\text{Ba}_2\text{Cu}_3\text{O}_{7-\delta}$.

Figure 4. Secondary electron images of several samples processed in the AAL. The large fraction of RE123 is evident in each micrograph. RE211 increases with increasing Y content of the bulk.

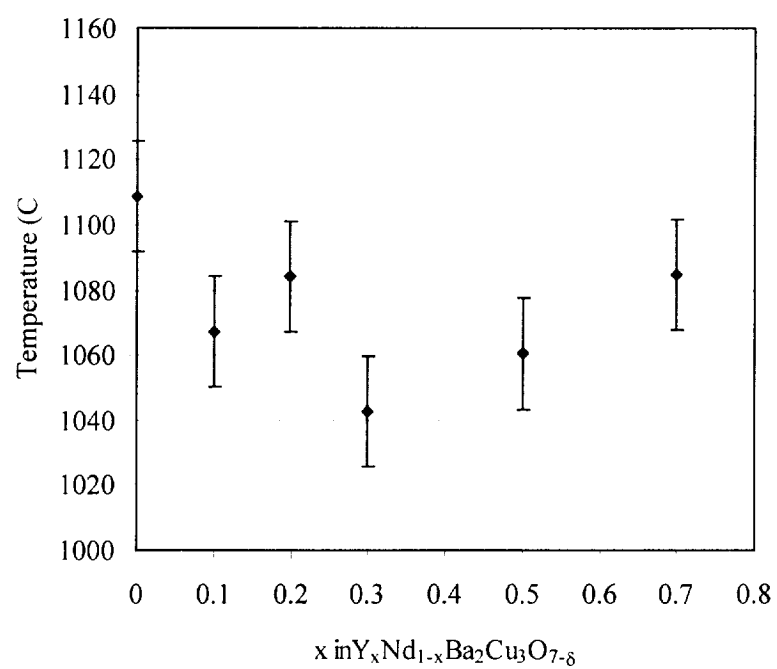


Figure 5. Experimentally determined average peritectic temperatures for Nd/Y123 binary alloy samples processed in the AAL. The temperature has been corrected using Nd123 as an in-situ calibration. The standard deviation in the data for multiple experiments with the same composition was used to calculate the magnitude of the error bars.

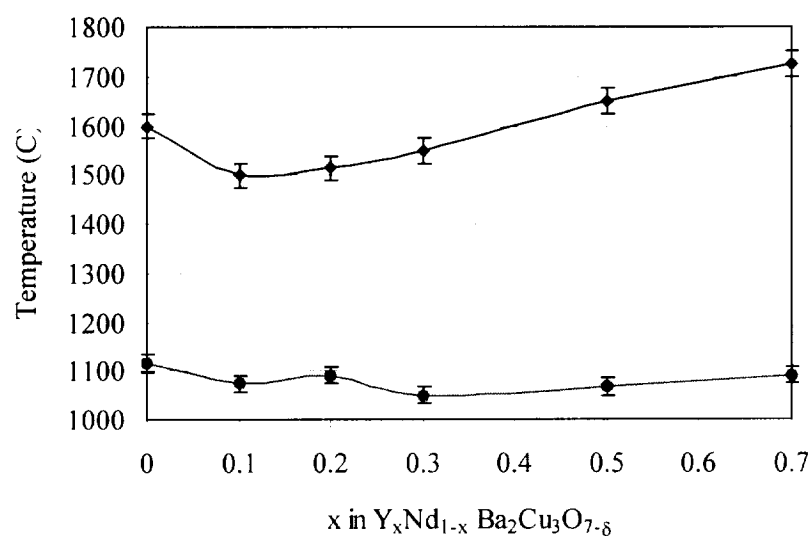


Figure 6. Trace of the Nd/Y123 liquidus and peritectic in pure O_2 . Liquidus temperatures were obtained from drop tube work performed by Olive and peritectic temperatures represent corrected experimental data from this work.¹³

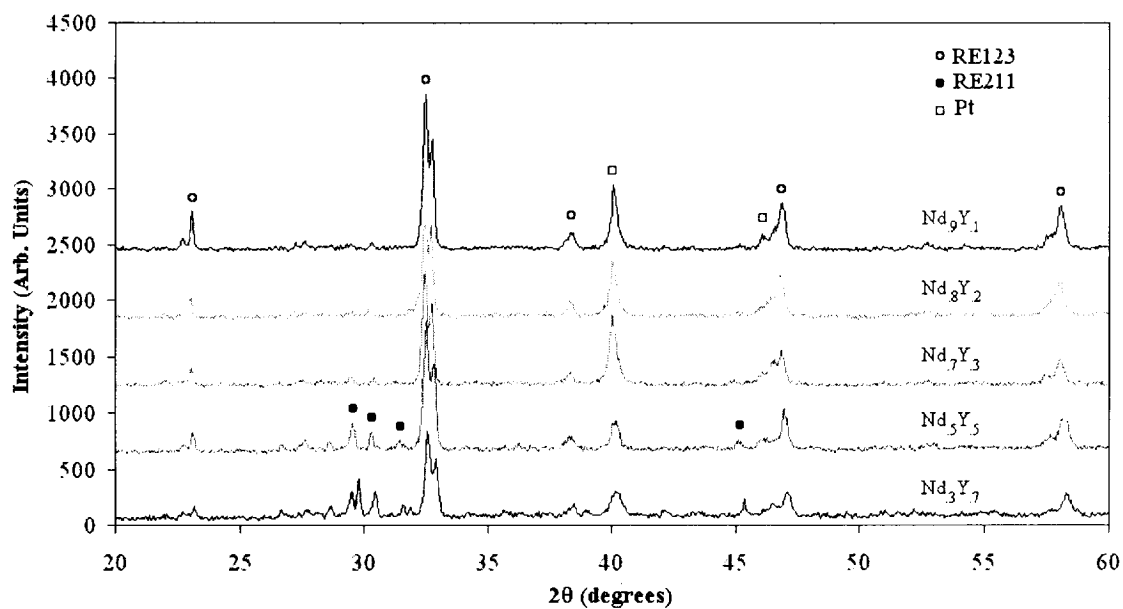


Figure 7. A compilation of XRD spectra for Y/Nd123 alloys processed in the AAL. RE123 is the dominant phase for all compositions. The appearance of RE211 in the scans becomes more prevalent in Y-rich compounds. The Pt peak is from the heating fixture in the XRD

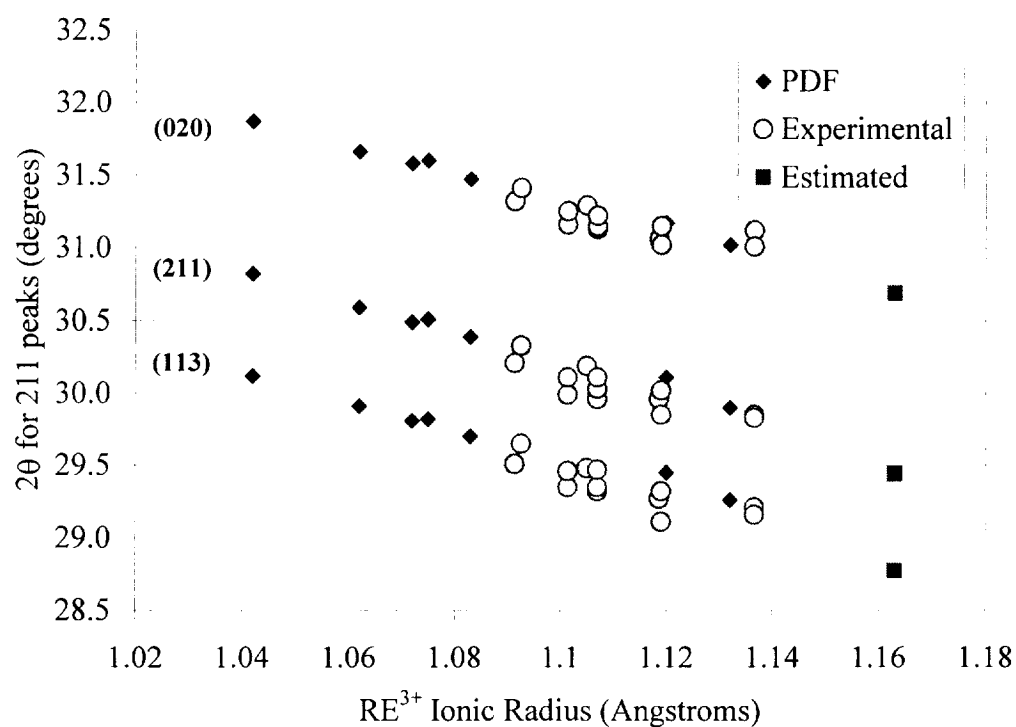


Figure 8. Comparison of the 2θ values for highest intensity diffraction planes for RE211 from powder diffraction files (RE = Dy, Er, Eu, Gd, Ho, Sm, Y, and Yb) with values from experimental data and theoretical values for Nd211 calculated from a simple model.

**Formation of $\text{NdBa}_2\text{Cu}_3\text{O}_{7-\delta}$ amorphous phase
by combining aero-acoustic levitation and splat quenching**

¹*K. Nagashio, ¹W. H. Hofmeister, ¹D. E. Gustafson, ¹A. Altgilbers, ¹R. J. Bayuzick
and ²K. Kuribayashi

¹Department of Chemical Engineering, Vanderbilt University
Nashville, Tennessee 37235, U.S.A

²The Institute of Space and Astronautical Science
3-3-1, Yoshinodai, Sagamihara, Kanagawa, 229-8510, JAPAN

[*nagashio@materials.isas.ac.jp](mailto:nagashio@materials.isas.ac.jp)

*Present address: The Institute of Space and Astronautical Science
3-3-1, Yoshinodai, Sagamihara, Kanagawa, 229-8510, JAPAN

Abstract

Small spherical samples (diameter~2mm) of $\text{NdBa}_2\text{Cu}_3\text{O}_{7-\delta}$ (Nd123) were fully melted in Ar gas flow in an aero-acoustic levitation device and subsequently rapidly cooled by splat quenching. For samples quenched above the liquidus, the microstructural and X-ray diffraction (XRD) observations suggested the existence of the amorphous phase with small quantities of the BaCuO_2 and BaCu_2O_x . The high temperature XRD results indicated that the decomposition of the amorphous phase, probably assisted by atmospheric CO_2 and H_2O , lead to formation of the BaCO_3 phase at 400 °C and, subsequently, the Nd123 phase was formed by the solid diffusion above 800 °C. Another set of Nd123 samples were fully melted in O_2 gas flow, undercooled while levitated, and then splat quenched at a temperature below the peritectic temperature (T_p). These samples possessed a microcrystalline microstructure of the Nd123 phase which was confirmed by XRD. This indicated that the Nd123 phase was solidified directly from the undercooled melt quenched below T_p .

Keywords: $\text{NdBa}_2\text{Cu}_3\text{O}_{7-\delta}$, containerless solidification, splat quench, amorphous, undercooling

I. INTRODUCTION

Applications of $\text{REBa}_2\text{Cu}_3\text{O}_{7-\delta}$ (RE123, RE=Y, Nd, Gd) superconducting oxides depend on enhancement of the critical current density (J_C). The J_C strongly depends on the microstructure derived from processing, while the critical temperature is a physical property of its material. Representative bulk processes for high J_C are quench & melt growth [1] and melt powder melt growth [2], where $\text{RE}_2\text{BaCuO}_5$ (RE211) phase is dispersed as a flux-pinning site in the RE123 matrix. It is, however, difficult to disperse the RE211 on a sufficiently fine scale due to the peritectic reaction.

Recently, in the $\text{Bi}_2\text{Sr}_2\text{CaCu}_2\text{O}_x$ (Bi2212) system, it was reported that single crystal doped with large amounts of Pb showed a drastic increase in J_C in an applied magnetic field [3]. Moreover, the fine dispersion of Pb in Bi2212 was examined by crystallization from an amorphous precursor [4]. Working with an amorphous precursor has a number of advantages, especially for peritectic systems, such as Fe-Nd-B [5]. In the Bi-system, the formation of the amorphous phase has been demonstrated by splat quenching [6], twin roller quenching [7] and containerless solidification [4, 8]. On the other hand, in the RE123 system, amorphous RE123 has hardly been reported. This mainly results from the difficulty of the complete melting of RE123 due to the high liquidus temperature (T_L), ~ 1800 K, compared with that of Bi2212, ~ 1200 K. At such a high temperature, a suitable crucible for the melt does not exist because of the strong reactivity of the melt and samples are easily contaminated. Furthermore, because of the gentle liquidus slope of the high temperature phase the temperature difference between T_L and T_C in Bi-system is very small, ~ 30 K, where T_C is the hypothetical congruent melting temperature of the peritectic phase. In case of RE123, the steep liquidus slope of the high temperature phase suggests a large difference between T_L and T_C , ~ 300 K,

which makes it difficult to undercool the RE123 melt below the glass transition temperature. The crystallization temperature for the amorphous phase is expected to be considerably lower than the peritectic temperature (T_p).

Recently, the rapid solidification experiment of Nd123 and Gd123 has been addressed above T_L by combining the drop tube processing and melt spinning technique [9-11]. It was suggested that the amorphous phase was obtained and the Nd123 phase crystallized from the amorphous phase around 630 °C by high temperature X-ray diffraction (HTXRD) at heating condition of 6.5 °C/min. The formation of Y123, however, has been reported by a sintering method using the powder precursors of Y_2O_3 , $BaCO_3$ and CuO with almost the same heating condition [12]. Therefore, the crystallization path from the amorphous phase cannot be delineated by HTXRD at heating rates of 6.5 °C/min.

In the present paper, the rapid solidification of Nd123 melts was carried out by combining an aero-acoustic levitator (AAL) and splat quenching system in order to obtain the RE123 amorphous phase and to elucidate the crystallization from the amorphous phase. The crystallization from the amorphous phase is discussed by the detailed observation of the microstructure as well as HTXRD. Additionally, melts quenched at temperatures below T_p formed the Nd123 phase directly from the melt, bypassing the peritectic reaction path and amorphous phase formation.

II. EXPERIMENTAL

The AAL with the splat quenching system is shown schematically in Fig. 1. It combines the containerless processing and the splat quenching technique to allow sample quenching at different

undercoolings. Copper anvils of 20 mm diameter with polished surfaces were used to enhance the cooling rate of the quenched specimens. The pneumatic pistons are driven by fast air valves triggered on the same circuit as the laser beam shutter.

In the present experiment, the spherical specimens with experimental composition of Nd123 and $\text{Nd}_3\text{Ba}_6\text{Cu}_{11}\text{O}_x$ (hyperperitectic composition) were prepared by laser hearth melting of powders. They were levitated by the AAL in Ar gas flow and heated above T_L by CO_2 laser. Then, the melt was quenched at a gas piston pressure of 0.65 MPa. The processed sample thickness was 20~50 μm . Alternatively, the Nd123 specimen levitated in O_2 gas flow was heated above T_L to achieve complete melting and undercooled below T_P (1112 $^\circ\text{C}$ in O_2 [13, 14]). Then, the Nd123 melt was quenched at the temperatures below T_P . Temperature measurements were performed with a two-color high-speed pyrometer with central wavelengths of 0.90 and 1.55 μm and a spot diameter of 1 mm. The reported accuracy of the pyrometer is $\pm 0.5\%$ of the measured values. The response time of the pyrometer is 2.0 ms, and a sampling rate of 1000 Hz was used for the data acquisition system.

Structural phase transitions were studied using a Scintag X_1 θ/θ automated powder diffractometer with a Cu target, Peltier cooled solid-state detector, and a Micristar high-temperature stage. Specimens were mounted on a Si (510) substrate and heated from room temperature to 900 $^\circ\text{C}$ at 30 $^\circ\text{C}/\text{min}$ by the Pt heater. The high temperature X-ray diffraction (HTXRD) measurements were performed at intervals of 100 $^\circ\text{C}$ after 1 min wait to ensure temperature equilibrium over a 2θ range of 22.5 $^\circ$ -37.5 $^\circ$ with 0.05 $^\circ$ resolution at a scan rate of 0.05 $^\circ/\text{s}$ in dry air.

The quenched specimens were annealed at 700 $^\circ\text{C}$ for 1 and 24 hours and at 1000 $^\circ\text{C}$ for 1 hour in air. Phase determination was carried out by powder X-ray diffraction (XRD) at a slow scan rate of 0.025 $^\circ/\text{s}$. The specimens quenched above T_L in Ar were polished by diamond paste with

lubricant of oil. The microstructure was characterized by a scanning electron microscopy (SEM) coupled with energy-dispersive spectroscopy (EDS).

III. RESULTS

Figure 2 shows the typical temperature vs time profile, where one was quenched above T_L and the other below T_p . The levitated specimens were heated or cooled as slow as possible to reduce the temperature gradient inside the specimens due to the low thermal conductivity. Therefore, surface temperature measured by the pyrometer is close to the temperature of the center. The splat-quenched materials typically resulted in plate with approximate dimensions of 1.5 mm diameter and 20~50 μm thickness as shown in Fig. 3. The maximum cooling rate was achieved around the center of specimen. Therefore, only central parts of processed specimens were chosen for analysis by SEM and XRD.

The HTXRD results of the specimen quenched above T_L in Ar are shown in Fig. 4. The BaCuO_2 and BaCu_2O_x phases are seen in the starting material, but disappeared at 400 °C. Thereafter, the BaCO_3 phase appeared. The peaks of the Nd_2CuO_4 and CuO phases were found at 600 °C and the BaCO_3 peaks increased in the intensity. Upon further heating the Nd123 phase appeared at 800 °C. The peaks of the BaCO_3 phase decreased at 900 °C, while the peak intensity of the Nd123 phase increased.

Figure 5 presents the XRD results of the specimens quenched in Ar at the slow scan rate of 0.025 °/s to elucidate the reaction pathway of the Nd123 phase in detail. As shown by the HTXRD results, BaCuO_2 and BaCu_2O_x phases were found at room temperature (a). The same specimen was heated

directly to 600 °C at 30 °C/s in dry air in the HTXRD apparatus and the diffraction pattern was measured. The peaks of the Nd_2CuO_4 and CuO phases appeared in addition to the largest peak of the BaCO_3 phase (b). In contrast with the strong peaks of the BaCO_3 phase, low intensity of the Ba-Cu-O phases at room temperature suggests the low volume fraction of the Ba-Cu-O phases. Alternatively, in the specimen annealed for 24 hours at 700 °C in dry air, the peaks of the Nd123 phase were the strongest feature, with a weak set of lines for the BaCuO_2 phase (c). In the specimen annealed for 1 hour at 1000 °C, the Nd123 peaks were found with the smaller full-width at half maximum than that at 700°C (d). Although the intense peak of Pt was indicated around 40° and 47° as appeared in Fig. 5c and 5d, this caused from the contamination of Pt on the Si substrate due to Pt heater. These Pt peaks were often observed because of the small amount of the sample obtained.

Figure 6 shows the SEM micrograph of the specimen quenched above T_L in Ar. In the specimen polished perpendicular to the splat surface, a uniform microstructure with the Nd123 composition was obtained. The specimens quenched above T_L in Ar were annealed at 700 °C and 1000 °C for 1 hour in dry air and polished parallel to the splat surface. Figure 7 shows the SEM micrographs of the annealed specimens. These micrographs are shown at the same magnification to reveal the microstructure transition more easily. Although the XRD results indicated the existence of the BaCuO_2 and BaCu_2O_x phases at the room temperature, these phases were not detected by the microstructure observation (a). The smooth surface observed at room temperature changed the rough surface in the specimen annealed at 700 °C (b). Table I gives the EDS results of the regions A, B and C collected by the size of white box indicated at the right side of bottom in Fig. 7b. Even the smooth surface region A has different composition from stoichiometric Nd123. In the region B, decrease of Ba content was indicated. Moreover, the small amount of flower-like Nd123 phase was observed in the region C containing almost no Ba content by EDS. The HTXRD results indicated

the existence of the BaCO_3 phase, which could not be detected in the microstructure. When the region B in Fig. 7b was magnified, a large amount of the small particles (~ 100 nm in diameter) were observed. However, the EDS analysis could not be carried out on these small particles. The specimen annealed at 1000°C indicated the smooth surface of the Nd123 phase without the substitution of Nd and Ba atoms (c). This was in good agreement with the XRD result of Fig. 5d.

The specimens were annealed at 700°C for 24 hours in air for further detailed observation. Figure 8 shows the SEM micrograph of the specimen polished parallel to the splat surface. Typical microstructure was flower-like Nd123 phase in Fig. 8a. This microstructure was detected in the region C of Fig. 7b. The small cylindrical Nd123 phase (b) was observed in the part indicated by white arrow in Fig. 8a. Moreover, the Nd_2CuO_4 phase (c) was found around the Nd123 cylindrical particles.

As the microstructures and the XRD results of Nd123 quenched above T_L in Ar gas flow are shown from Fig. 4 to Fig. 8, the similar phase transition was observed in the hyperperitectic-Nd123 quenched above T_L in Ar. Note that the smooth surface observed in the hyper-Nd123 specimen at room temperature had the same composition as the initial composition.

Figure 9 exhibits the XRD results of specimen quenched in O_2 gas flow at 993°C , which is below T_P . The intense peak of the Nd123 phase was observed. The peaks of the high temperature phases, Nd422 and Nd_2O_3 phases, were not found in the XRD results. The microstructure of the specimen quenched at 981°C is shown in Fig. 10. In the specimen polished perpendicular to the splat surface, single phase Nd123 was found. This is consistent with the XRD result. In the specimen quenched at 1165°C , 53°C above T_P , microstructural transition from fine to coarse grain of the Nd123 phase was observed from the edge to the center. That is, although grain boundary of the single phase Nd123 in Fig. 10 is not discernable with the resolution in the SEM, it can be seen

that very fine microcrystalline Nd123 was obtained all through the specimen by quenching at large enough undercooling below T_p .

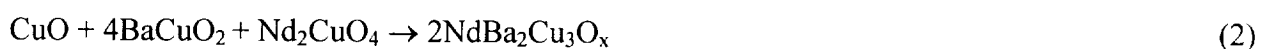
IV. DISCUSSION

Samples of Nd123 were heated above T_L in Ar gas flow and rapidly quenched by combining AAL and splat quenching. The amorphous-like phase with the Nd123 composition was observed in Fig. 6. The XRD result at the room temperature (Fig. 5a), however, showed the very low peaks of the $BaCuO_2$ and $BaCu_2O_2$ phases in contrast with the strong peaks of the $BaCO_3$ phase at 600 °C (Fig. 5b), while the stable phases, Nd_2O_3 , $Nd_4Ba_2Cu_2O_{10}$ (Nd422) and Nd123 were completely suppressed. Moreover, the amorphous-like phase was more reactive to the atmospheric gasses than the Nd123 phase, which is subject to decomposition [15]. Increase of area exposed to atmosphere by crushing the sample for the preparation of XRD seemed to rapidly induce the decomposition of amorphous-like phase. This is also associated with the fact that XRD results at room temperature did not indicate any distinct features of the amorphous phase. Furthermore, in the hyperperitectic-Nd123 specimen, the amorphous-like phase with the same composition as the initial melt was observed. That is, these results conclude that the featureless phase obtained by the splat quenching above T_L in Ar gas flow is the amorphous Nd123 including very low amount of the Ba-Cu-O phases.

The HTXRD results of Fig. 4 indicated that the $BaCO_3$ phase appeared at 400 °C before the peaks of the Nd123 phase was observed at 800 °C. Ba atom in the amorphous seems to decompose into the $Ba(OH)_2$ phase due to the instability to the atmospheric water vapor. Subsequently, the

Ba(OH)₂ phase may react with CO₂ in atmosphere according to the heating around 400 °C and lead to the intense peaks of the BaCO₃ phase. Moreover, EDS results of the rough surface as shown in Fig. 7b indicated that the composition of the rough part, which included the large amount of small particles, was different from the stoichiometric Nd123 composition. This means that the Nd123 phase did not crystallize from the amorphous, although the smooth surface of the Nd123 phase (Fig. 7b) was observed in the specimen annealed at 1000 °C. The microstructure transition with an increase of the annealing temperature as well as the HTXRD results indicated that the amorphous decomposed due to the instability to the atmospheric gasses and leads to the appearance of the BaCO₃ phase and, finally, the Nd123 phase was formed by the solid diffusion around 800 °C, not by the crystallization from the amorphous. Although Folkerts et al. have reported the crystallization of the Nd123 phase from the amorphous by the HTXRD results, it may be misidentified because they did not carry out the HTXRD scan of 20~25° containing the most intense peak of the BaCO₃ phase [9-11].

As discussed above, the experimental results indicated the amorphous phase immediately decomposed and lead to the BaCO₃ phase by the reaction with CO₂ although the amorphous phase was formed in the specimen splat-quenched in Ar. The subsequent reaction pathway for the Nd123 formation was discussed. The HTXRD result at 600 °C of Fig. 5b indicates the stable phases after the decomposition of the amorphous phase are the BaCO₃, CuO and Nd₂CuO₄ phases. Furthermore, the XRD result of the sample annealed for 24 hours suggests that the BaCuO₂ phase is an intermediate phase formed by the BaCO₃ and CuO phases for the formation of the Nd123 phase. The reaction pathway for the Nd123 formation in dry air is considered as follows,



The decomposition temperature of the BaCO_3 phase observed in Fig. 3 was consistent with the report that the decomposition of the BaCO_3 phase take place around 800 °C in air [16]. Moreover, it is well known that the Y123 phase decomposes to the Y211, Ba(OH)_2 and CuO phases by the reaction with H_2O [17]. In the present experiment, however, the Nd422 phase was not observed. Therefore, the identification of the Nd_2CuO_4 phase by SEM (Fig. 8c) as well as XRD replaces Nd422 phase and suggests that Ba atom in the obtained amorphous phase mostly reacted to the BaCO_3 phase. The BaCO_3 phase, however, may be removed by polishing, because rough spots with almost no Ba content were detected by SEM as shown in Fig. 7b. Therefore, after the decomposition of the amorphous, the reaction pathway for the Nd123 formation results in the reactions (1) and (2). Moreover, the nucleation of the Nd123 phase seems to take place on the Nd_2CuO_4 phase with a tetragonal structure, because the BaCuO_2 and CuO phases are cubic and monoclinic structure, respectively. Subsequently, the Nd123 phase formed small cylindrical particles and they combined as flower-like structures, as shown in Fig. 8. This flower-like particle was also observed in the region C (Fig. 7b) in the sample annealed at 700 °C for 1 hour. The formation of Nd123 phase progressed at region C of the most reactive region and resulted in the cylindrical particles in Fig. 8b. Finally, the flower-like particles grew to lead to the smooth surface of Fig. 7c as the annealing temperature increased toward 800 °C.

In the case of the splat quenching below T_P , uniform Nd123 microstructure was obtained. The peaks of the high temperature phases, Nd_2O_3 and Nd422, were not detected by XRD. This indicated that the Nd123 phase was solidified directly from the undercooled melt by quenched below T_P . The author's has already reported the direct growth of the Nd123 phase from the undercooled melt using AAL or drop tube [18-21]. In the previous instances, the Nd123 phase grew dendritically. The very fine microcrystalline Nd123 microstructure in the present experiment is expected to lead to the

enhancement of physical properties, such as J_C .

The crystallization of the Nd123 phase was observed in the specimen quenched below T_P , while amorphous Nd123 was obtained in the specimen quenched above T_L . This is comprehended by the consideration based on the continuous-cooling-transformation (CCT) diagram as shown schematically in Fig. 11. This CCT diagram is illustrated at the cooling rates acquired in the general quenching experiments, because each cooling rate was not measured in the present experiment. The undercooling below T_P of the liquid prior to splat quenching does not favor glass formation because there is sufficient time for a near-equilibrium distribution of sub-critical embryos to develop in the liquid during undercooling [22].

V. CONCLUSIONS

Splat quenching experiments were conducted on the superconducting oxide, Nd123, in Ar or O₂ gas flow using an aero-acoustic levitator with splat quenching system. The amorphous Nd123 was observed in the specimen quenched above the liquidus temperature in Ar. The amorphous decomposed due to the instability to the atmospheric vapor and lead to the appearance of the BaCO₃, Nd₂CuO₄ and CuO phases above 400 °C by the reaction with CO₂, as indicated by high temperature X-ray diffraction result. Subsequently, the Nd123 phase was formed around 800 °C by the solid diffusion of their phases. Moreover, microstructure transition of the Nd123 phase from cylindrical to flower-like particles was observed through the solid diffusion. On the other hand, the undercooled Nd123 melt, (cooled in O₂) and splat quenched below its peritectic temperature did not form the amorphous phase. Microcrystalline Nd123 was found. This indicated that the Nd123 phase

was solidified directly from the undercooled melt by quenching below T_p .

ACKNOWLEDGEMENT

The authors gratefully acknowledge the support of the NASA Microgravity Science and Applications Division under NASA Grant No. NAG8-1275. This work was financially supported by a Grant-in Aid for Scientific Research from The Ministry of Education, Science, Sports and Culture and the project of Core Research for Evolutional Science and Technology (CREST). This research was partly supported by Research Fellowships of the Japan Society for the Promotion of Science for Young Scientists. The authors acknowledge the help of Dr. Richard Weber of Containerless Research, Inc. for his help in combining the splat quench apparatus with the Aero Acoustic Levitator, and assistance with the undercooled splat quench experiments.

REFERENCES

- [1] M. Murakami, M. Morita and N. Koyama, *Jpn. J. Appl. Phys.* **28**, L1125 (1989).
- [2] H. Fujimoto, M. Murakami, S. Gotoh, N. Koshizuka, T. Oyama, Y. Shiohara and S. Tanaka, In: *Advances in Superconductivity – II*, Proc. 2nd. Int. Symp. On Superconductivity, 1989, p.285.
- [3] I. Chong, Z. Hiroi, M. Izumi, J. Shimoyama, Y. Nakayama, K. Kishio, T. Terashima, Y. Bando and M. Takano, *Science* **276**, 770 (1997).
- [4] Y. Hishinuma, H. Fujii, A. Matsumoto, K. Hirata, H. Takeya, H. Kumakura and K. Togano, *Jpn. J. Appl. Phys.* **37**, L859 (1998).
- [5] T. Harada and T. Kuji, *J. Mater. Res.* **9**, 372 (1994).
- [6] T. G. Holesinger, D. J. Miller and L. S. Chumbley, *J. Mater. Res.* **7**, 1658 (1992).
- [7] K. Nassau, A. E. Miller, E. M. Gyorgy and T. Siegrist, *J. Mater. Res.* **4**, 1330 (1989).
- [8] M. J. Kramer, L. Margulies, S. R. Arrasmith, K. W. Dennis, J. C. Lang, R. W. McCallum and P. K. Gallagher, *J. Mater. Res.* **9**, 1661 (1994).
- [9] T. J. Folkerts, S. I. Yoo, Youwen Xu, M. J. Kramer, K. W. Dennis and R. W. McCallum, In: D. T. Shaw, C. C. Tsuei, T. R. Schneider, Y. Shiohara (Ed.), *Layered Superconductors: Fabrication, Properties and Applications*, Mat. Res. Soc. Symp. Proc., San Francisco, California, **275**, 335 (1992).
- [10] T. J. Folkerts, K. W. Dennis, S. I. Yoo, Youwen Xu, M. J. Kramer and R. W. McCallum, *IEEE Trans. Appl. Super.* **3**, 1150 (1993).
- [11] R. W. McCallum, M. J. Kramer, T. J. Folkerts, S. R. Arrasmith, B. D. Merkle, S. I. Yoo, Youwen Xu and K. W. Dennis, In: S. K. Malik and S. S. Shah (Ed.), *Physical and Material Properties of High Temperature Superconductors*, Nova Science Publishers, New York, 1993, p. 667.
- [12] V. Milonopoulou, K. M. Forster, J. P. Formica, J. Kulik, T. J. Richardson and D. Luss, *J. Mater. Res.* **9**, 275 (1994).
- [13] M. Yoshizumi, M. Kambara, Y. Shiohara and T. Umeda, *Physica C* **334**, 77 (2000).
- [14] M. Kambara, M. Nakamura, Y. Shiohara and T. Umeda, *Physica C* **275**, 127 (1997).
- [15] Y. Shiohara, ISTEK, private communication.
- [16] H. M. O'Bryan and P. K. Gallagher, In: M. F. Yan (Ed.), *Ceramic Superconductors II*, American Ceramic Society, Westerville, OH, 1988, p. 89.
- [17] M. F. Yan, R. L. Barns, H. M. O'Bryan, Jr., P. K. Gallagher, R. C. Sherwood and S. Jin, *Appl. Phys. Lett.* **51**, 532 (1987).
- [18] J. R. Olive, W. H. Hofmeister, R. J. Bayuzick and M. Vlasse, *J. Mater. Res.* **14**, 3843 (1999).
- [19] J. R. Olive, W. H. Hofmeister, R. J. Bayuzick and M. Vlasse, *J. Mater. Res.* **14**, 3851 (1999).
- [20] K. Nagashio, Y. Takamura, K. Kuribayashi and Y. Shiohara, *J. Crystal Growth* **200**, 118 (1999).
- [21] K. Nagashio, K. Kuribayashi and Y. Takamura, *Acta mater.* **48**, 3049 (2000).
- [22] G. A. Bertero, W. H. Hofmeister, M. B. Robinson and R. J. Bayuzick, *Metall. Trans. A* **22A**, 2713 (1991).

Figures

- Figure 1. Schematic of an aero-acoustic levitator and splat quenching system. Complete melting of the sample was achieved by CO₂ laser.
- Figure 2. Typical temperature vs time profile. (a): quenched above T_L in Ar, and (b): quenched below T_P in O₂. The T_P reported in O₂ atmosphere is indicated in this figure.
- Figure 3. Low magnification micrograph of as-quenched specimen.
- Figure 4. High temperature X-ray results in dry air of specimen splat quenched above T_L in Ar.
- Figure 5. XRD patterns of the specimen quenched above T_L in Ar gas flow. (a): profile from the as-quenched specimen at RT, (b): HTXRD profile. This was obtained after heating specimen (a) directly to 600 °C at 30 °C/s in dry air, (c): profile from the specimen at RT after annealed at 700 °C for 24 hours in air, and (d): profile from the specimen at RT after annealing for 1 hours at 1000 °C.
- Figure 6. SEM micrograph of the specimen quenched above T_L in Ar. The cross-section of specimen quenched from the direction shown by white arrows.
- Figure 7. SEM micrographs of specimen annealed at different temperatures for 1 hour in air. (a): room temperature, (b): 700 °C, and (c): 1000 °C.
- Figure 8. SEM micrographs of specimen annealed for 24 hours in air.
- Figure 9. XRD result of the specimen quenched below T_P in O₂.
- Figure 10. SEM micrograph of the specimen quenched below T_P in O₂. The cross-section of specimen quenched from the direction shown by white arrows.
- Figure 11. Schematic of a continuous-cooling-transformation diagram.
- Table I. EDS results of the regions indicated in Fig. 7b.

Figure 1

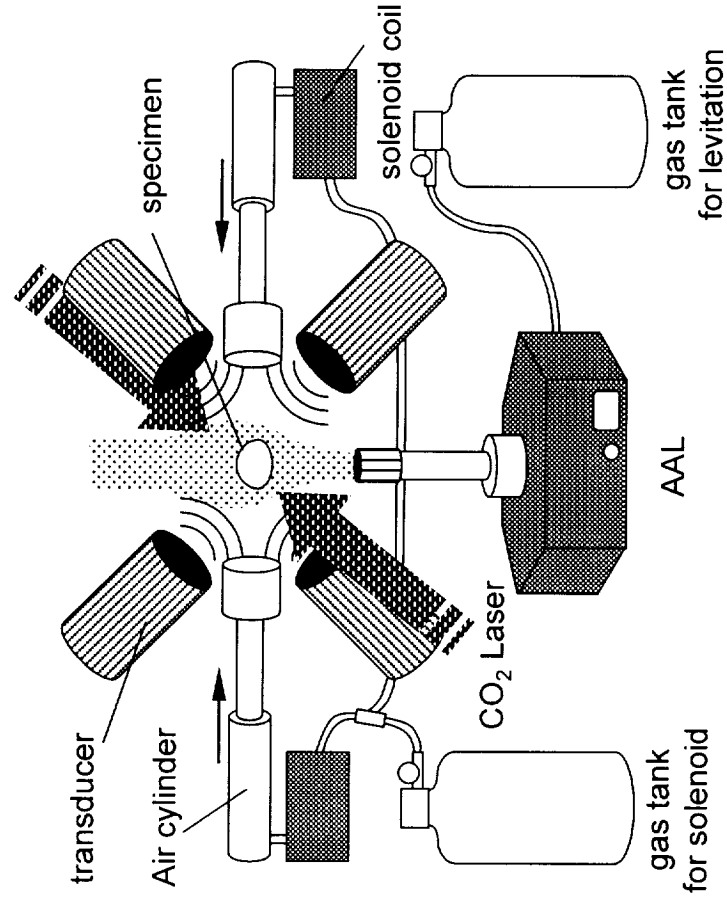


Figure 1. Schematic of an aero-acoustic levitator and splat quenching system. Complete melting of the sample is achieved by CO₂ laser.

Figure 2

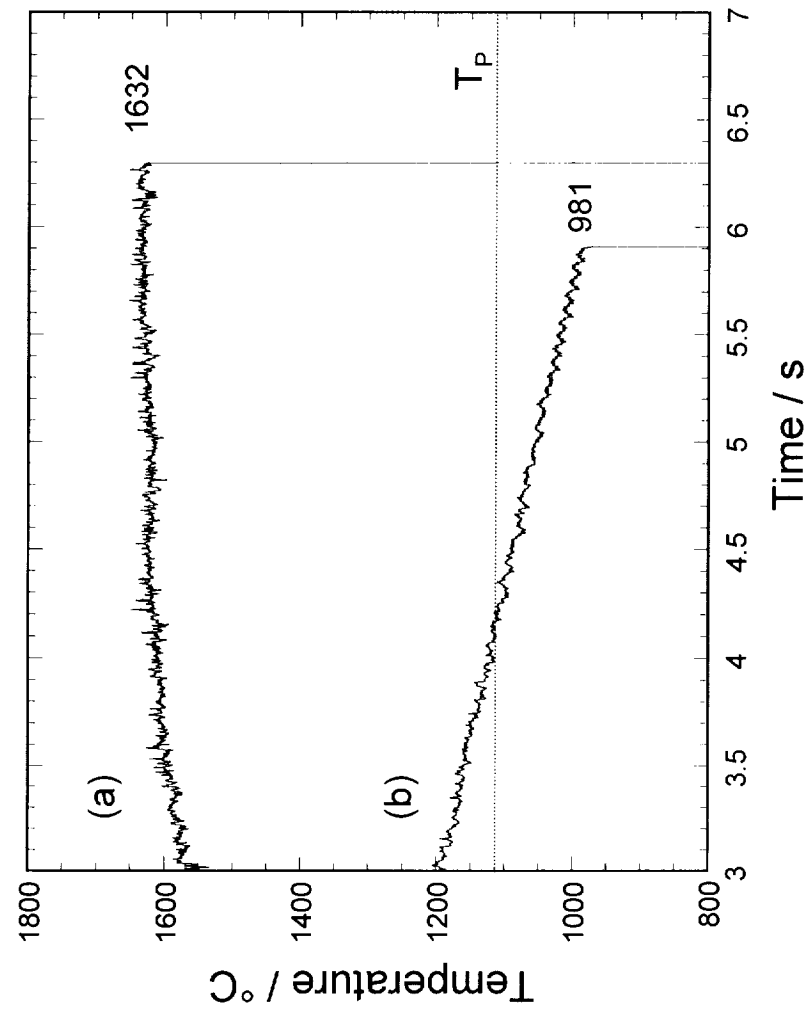


Figure 2 Typical temperature vs time profile. (a) quenched above T_L in Ar. (b) quenched below T_P in O_2 . T_P reported in O_2 atmosphere is indicated in this figure.

Figure 3

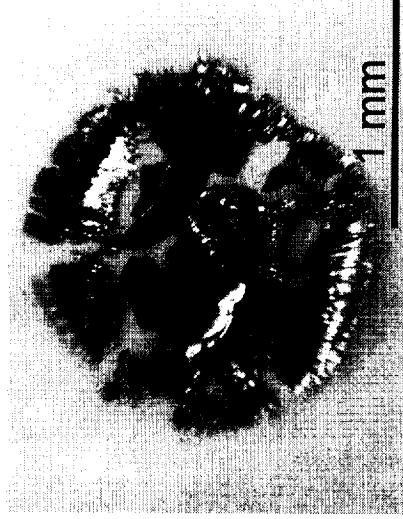


Figure 3 Low magnification micrograph of as-quenched specimen.

Figure 4

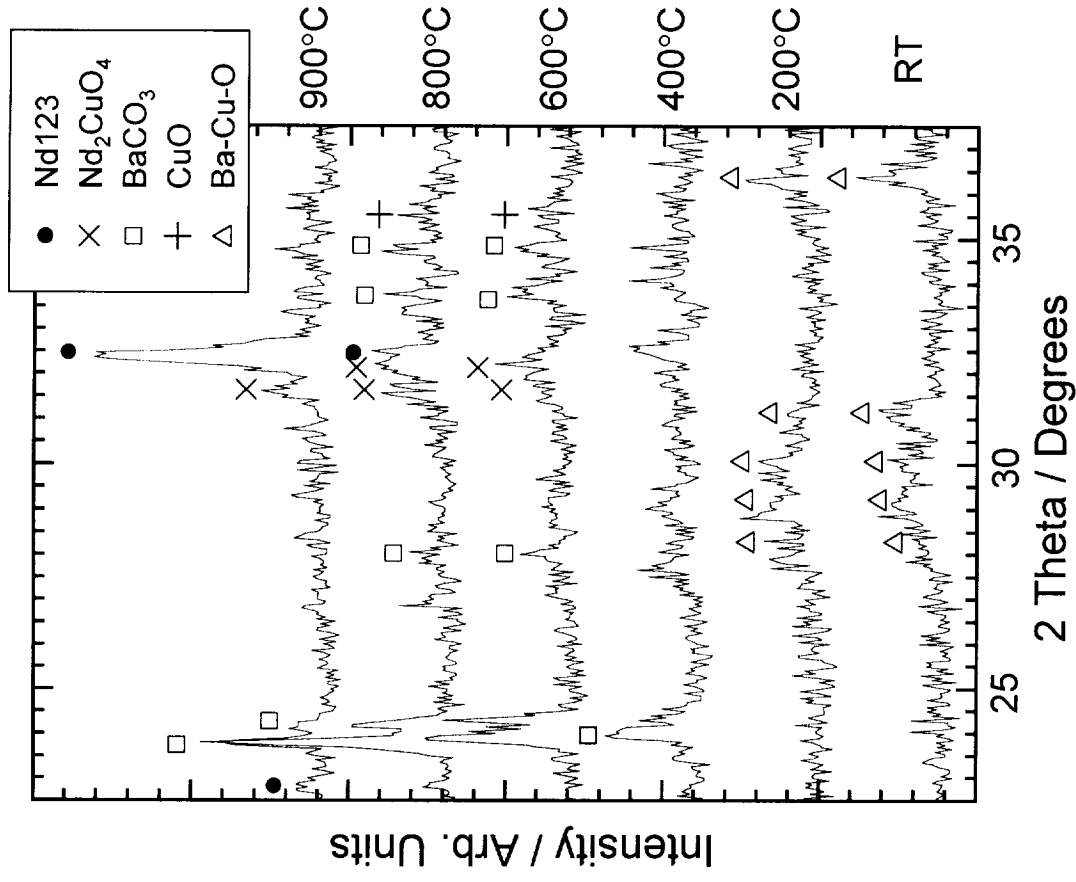


Figure 4. The HTXRD results in dry air of the specimen splat quenched above T_L in Ar.

Figure 5

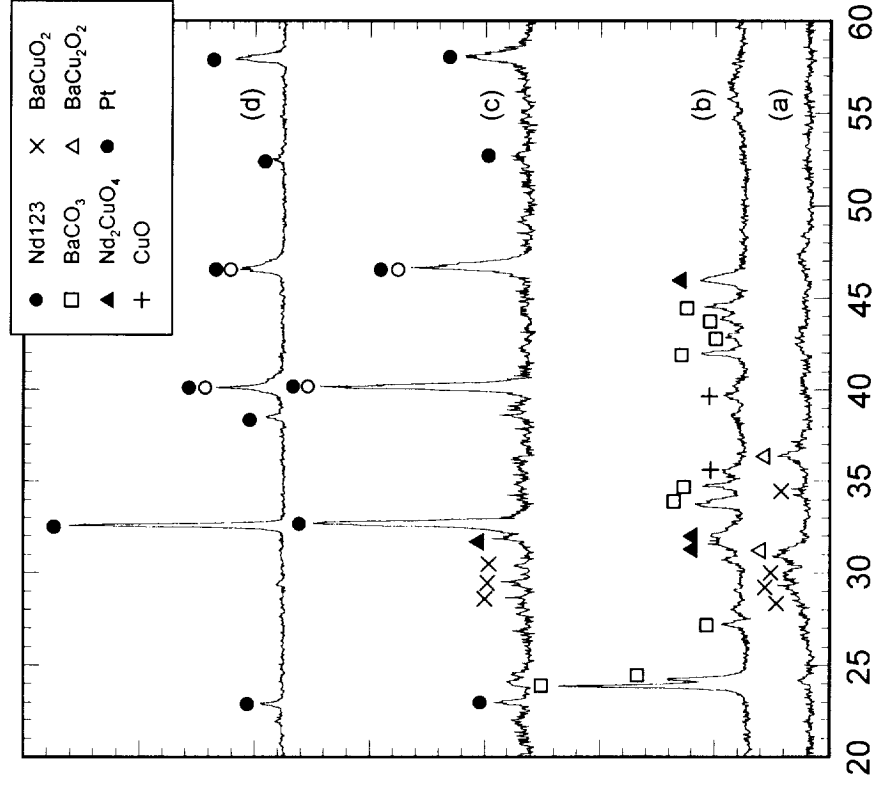


Figure 5. XRD patterns of the specimen quenched above T_L in Ar gas flow. (a): profile from the as-quenched specimen at RT, (b): HTXRD profile. This was obtained after heating specimen (a) directly to 600 °C at 30 °C/s in dry air, (c): profile from the specimen at RT after annealing at 700 °C for 24 hours in air, and (d): profile from the specimen at RT after annealing for 1 hours at 1000 °C.

Figure 6

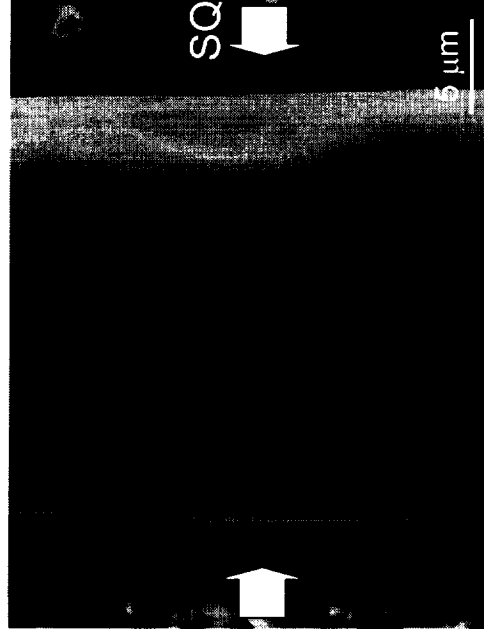


Figure 6. SEM micrograph of the specimen quenched above T_L in Ar. The cross-section of specimen quenched from the direction shown by white arrows.

Figure 7

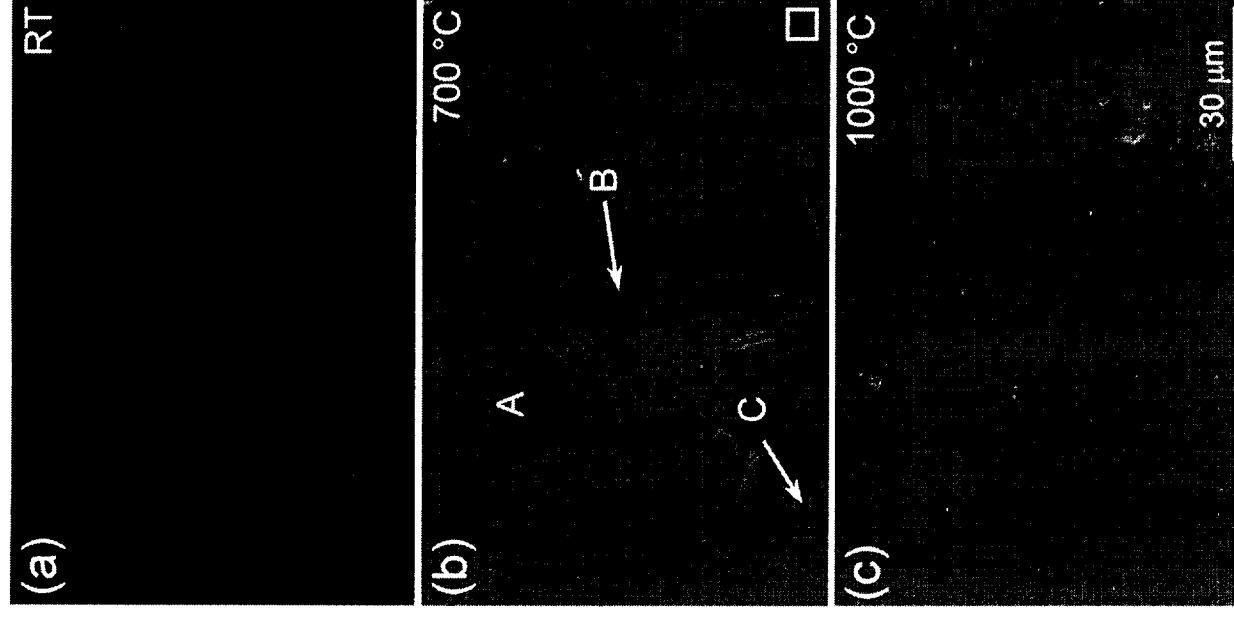


Figure 7. SEM micrographs of specimen annealed at different temperatures for 1 hour in air. (a): room temperature, (b): 700 °C, and (c): 1000 °C.

Figure 8

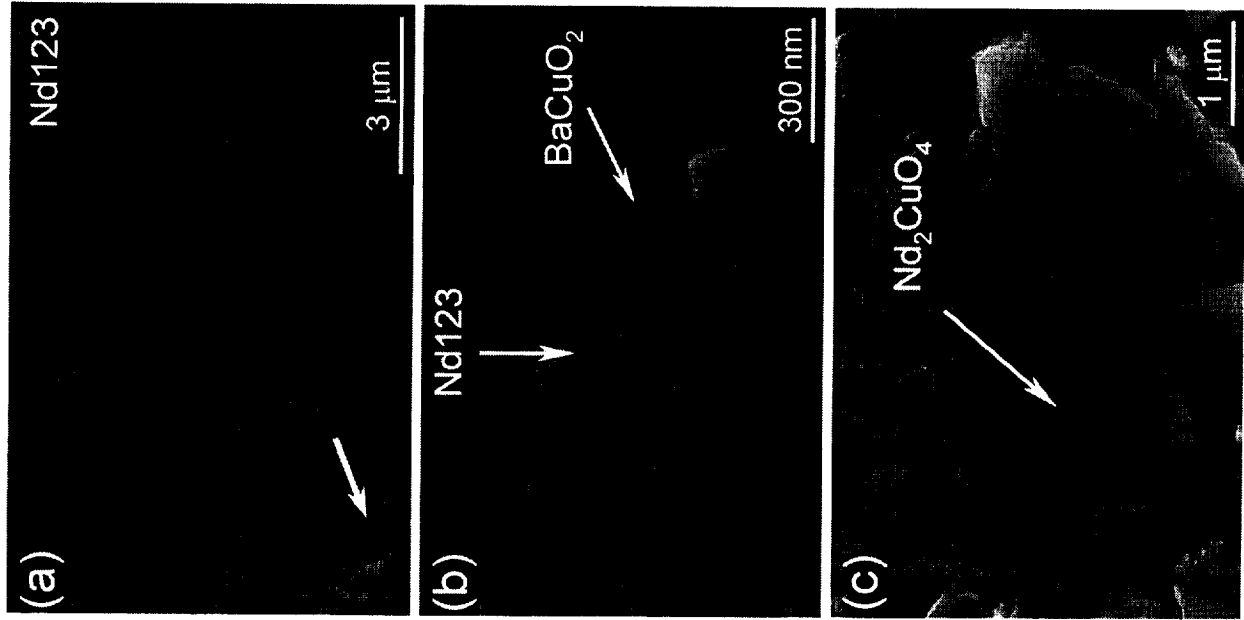


Figure 8 SEM micrographs of specimen annealed for 24 hours in air.

Figure 9

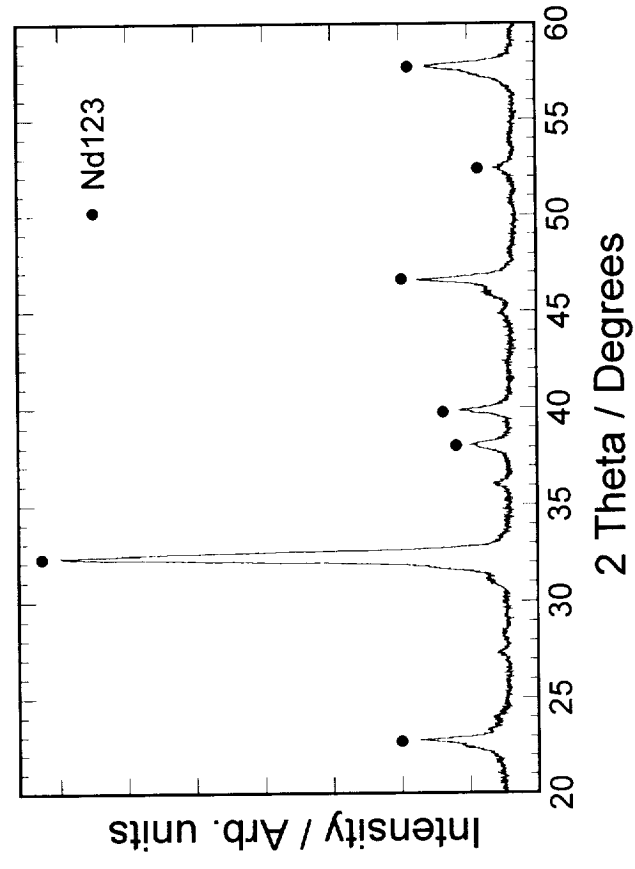


Figure 9. XRD result of the specimen quenched below T_p in O_2 .

Figure 10



Figure 10. SEM micrograph of the specimen quenched below T_p in O_2 . The cross-section of specimen quenched from the direction shown by white arrows.

Figure 11

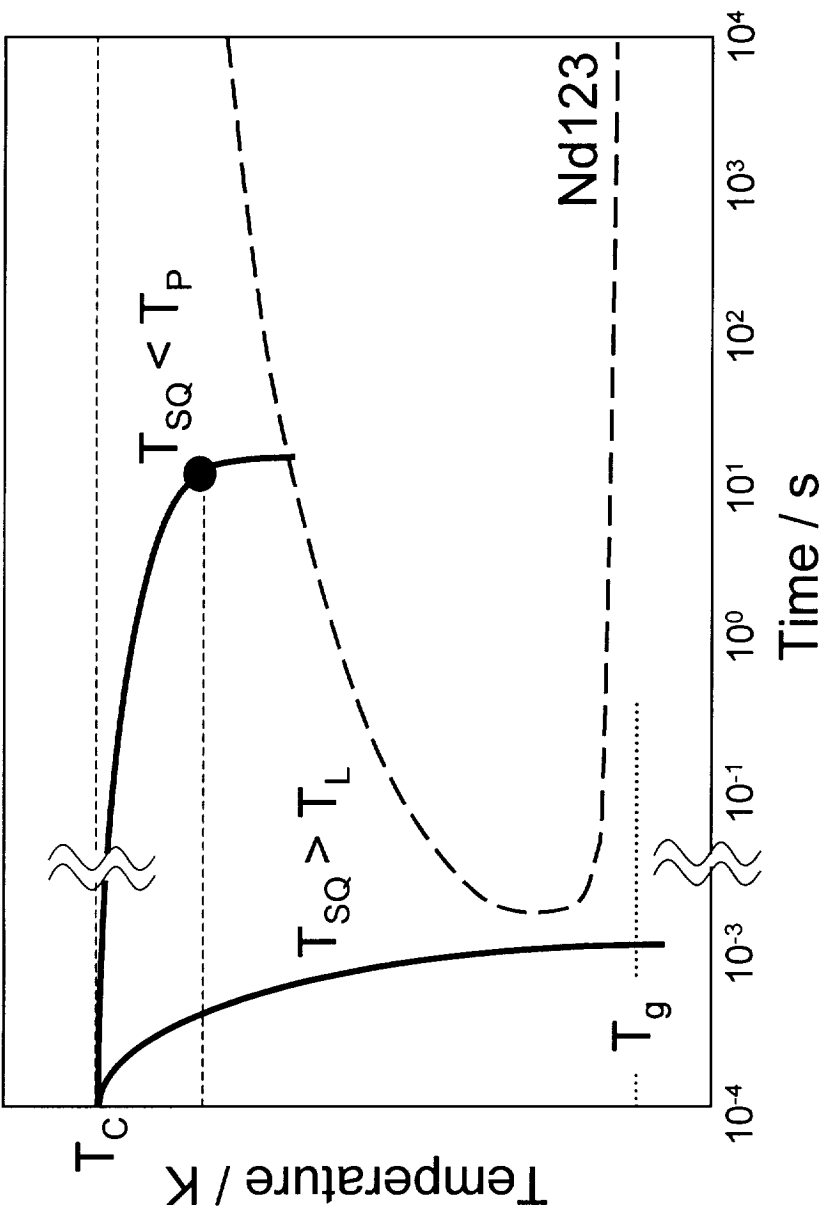


Figure 11. Schematic of a continuous-cooling-transformation diagram.

Table I

Table I. EDS results of the regions indicated in Fig. 7b.

	A	B	C
Nd	18.13	20.76	20.99
Ba	31.96	18.80	5.19
Cu	49.91	60.44	73.82